Flow, Turbulence and Combustion (2022) 108:263–301
https://doi.org/10.1007/s10494-021-00266-x

Effect of Fuel Stratification on OH and CH_2O PLIF Multiplication of Turbulent Hydrogen-Enriched Flames

S. Mohammadnejad[1] · L. Saca[1] · R. Heydarlaki[1] · Q. An[2] · P. Vena[2] · S. Yun[2] · P. Versailles[3] · G. Bourque[3,4] · S. Kheirkhah[1]

Received: 24 October 2020 / Accepted: 23 April 2021 / Published online: 12 May 2021

Abstract
Multiplication of hydroxyl and formaldehyde planar laser-induced fluorescence signals for turbulent hydrogen-enriched methane–air flames with compositionally inhomogeneous mixtures is investigated experimentally. Hydrogen-enriched methane–air flames with a global fuel–air equivalence ratio of 0.8 and hydrogen-enrichment percentage of 60% are examined. Two nozzles, each containing 4 fuel/air injection lobes are used in the experiments. The lobes of the first nozzle are straight, while those of the second nozzle are not, generating a swirling motion. The fuel is injected through several small diameter holes into the lobes. The amount of injected fuel flow rate varies between the lobes, generating stratified conditions. For each nozzle, two mean bulk flow velocities of 5 and 25 m/s are tested. Simultaneous hydroxyl and formaldehyde planar laser-induced fluorescence as well as separate stereoscopic particle image velocimetry are performed for the tested reacting conditions. For non-reacting flow tests, separate particle image velocimetry and acetone planar laser-induced fluorescence experiments are conducted to study the background turbulent flow characteristics and fuel/air mixing, respectively. The results show that stratification can lead to fragmentation of the flames and generation of islands with noticeable multiplication of hydroxyl and formaldehyde planar laser-induced fluorescence signals. Due to their significantly large number of occurrences, such flame structure can generate relatively large integral of the PLIF signals multiplication.

Keywords Stratified turbulent flames · Flames with compositionally inhomogeneous mixtures · Simultaneous OH/CH_2O PLIF and SPIV · Acetone PLIF

✉ S. Kheirkhah
sina.kheirkhah@ubc.ca

[1] School of Engineering, The University of British Columbia, Kelowna, BC V1V1V7, Canada

[2] Gas Turbine Laboratory, National Research Council Canada, Ottawa, ON K1A0R6, Canada

[3] Siemens Energy Canada Limited, Montreal, QC H9P1A5, Canada

[4] McGill University, Montreal, QC H3A0G4, Canada

1 Introduction

Gas turbine engines operate under premixed, partially-premixed, and/or non-premixed combustion modes. On one hand, non-premixed flames, compared to fully premixed flames, may feature relatively large combustion products temperature, which can lead to large amount of pollutants formation and emission, see for example (Moore 1997; Terasaki and Hayashi 1996; Hewson and Bollig 1996). On the other hand, fully premixed flames are susceptible to combustion instabilities, which are detrimental to the engine operation (Candel 1992; McManus et al. 1993; Lieuwen 2003). In order to address the emission and combustion instability issues, partial fuel and air mixing strategies are being implemented in gas turbine engine injectors. Such strategies lead to generation of turbulent partially premixed flames. As reviewed in Masri (2015), one category of turbulent partially premixed flames is turbulent premixed flames with compositionally inhomogeneous mixtures. These are also referred to as stratified turbulent flames. In this category of flames, the fuel and air are locally and fully mixed at molecular level; however, at larger scales, there exist inhomogeneities in spatial distribution of the fuel–air equivalence ratio. To the best knowledge of the authors, our understanding related to the effect of stratification on how fast turbulent premixed flames burn is limited and requires further investigations. In the following, the related literature for both turbulent premixed flames with compositionally homogeneous mixtures and with stratification is briefly reviewed.

For fully premixed flames, the rate at which reactants are converted to products (i.e. burning rate) depends on the internal flame structure (Borghi 1988; Driscoll 2008; Driscoll et al. 2020). The internal flame structure itself depends on the ratio of the chemical to flow timescales, which is referred to as the Karlovitz number (Ka). For relatively small Karlovitz numbers ($Ka \lesssim 50$), the internal structure (preheat and reaction layers) of the flames may remain thin and similar to that of the laminar counterpart (Borghi 1988; Driscoll 2008; Driscoll et al. 2020); however, phenomenon such as flame merging can lead to occasional thickening of the reaction layer (Mohammadnejad et al. 2019). For relatively large Karlovitz number flames ($Ka \gtrsim 50$), there exists a consensus in the literature that the preheat layer can increase to values several times that of the laminar premixed flame, see for example Skiba 2017; Skiba et al. 2018; Zhou et al. 2017; Mohammadnejad et al. 2020). However, there does not exist a consensus in the literature regarding the reaction layer thickness. Some investigations suggest that the reaction layer remains relatively thin (Driscoll et al. 2020; Skiba 2017; Skiba et al. 2018), but some (Mohammadnejad et al. 2020; Zhou et al. 2015a, b; Yuen and Gülder 2009; Dunn et al. 2007, 2009, 2010) reported that the reaction layer can become broadened/distributed, and its thickness can increase up to several times that of the laminar flame. A potential reason for the thickening of the reaction layer has been speculated to be due to the penetration of small-scale eddies into the reaction layer (Borghi 1988; Mohammadnejad et al. 2020; Zimont 1979; Gülder 2007). However, to the best knowledge of the authors, this is not experimentally demonstrated yet. The Direct Numerical Simulation (DNS) studies of Lapointe et al. (2015), Wang et al. (2017, 2018) suggest that, for large Karlovitz numbers, small scale eddies may penetrate into the reaction layer, altering the flame structure. However, compared to the studies of Lapointe et al. (2015), Wang et al. (2017, 2018), DNS of Aspden et al. (2011a, 2011b, 2019) suggests reaction layer broadening of the methane/air turbulent premixed flames only occurs for $Ka \gtrsim 9000$.

Understanding the internal structure of premixed flames is of prime importance as it allows for development of physics-based models which facilitate accurate estimation of the

burning rate. For small Karlovitz number flames, the reaction layer is relatively thin, it propagates at the laminar flame speed corrected for the effect of stretch Driscoll (2008), and can be estimated using imaging diagnostics such as Mie (Gouldin and Miles 1995; Bourguignon et al. 1996; Guo et al. 2010; Kheirkhah and Gülder 2015; Kheirkhah 2016), and Rayleigh (Plessing et al. 2000; Tamadonfar and Gülder 2016) scattering. Compared to these diagnostics, simultaneous Planar Laser-Induced Fluorescence (PLIF) of CH radical (see the studies of Carter and collaborators (Carter et al. 2016; Skiba et al. 2017; Filatyev et al. 2005), as well as the multiplication of OH and formaldehyde (CH_2O) PLIF signals is also utilized in past investigations (see, e.g. Mohammadnejad et al. 2019; Skiba et al. 2019; Sjöholm et al. 2013; Osborne et al. 2016) to visualize the reaction zone. OH radical and formaldehyde molecule can provide insight into the flame structure. Specifically, the thresholded formaldehyde and $OH \times CH_2O$ PLIF signals are used for detecting the preheat and reaction layer thicknesses, respectively, see for example (Zhou et al. 2017; Skiba et al. 2016; Mohammadnejad et al. 2020). For both small and large Karlovitz number turbulent premixed flames with compositionally homogeneous mixtures, the direct numerical simulations of several past investigations, see for example (Najm et al. 1998; Haworth et al. 2000), suggest that the multiplication of OH and CH_2O mass and/or mole fractions is a good indicator of the heat release rate, which is equivalent to the burning rate. However, the accuracy of $OH \times CH_2O$ PLIF signals for visualizing the heat release rate can be influenced by several parameters such as imaging resolution, the utilized filtering schemes, and laser sheet thickness (Wabel et al. 2018). Also, in addition to reaction of OH and formaldehyde which generates HCO (contributes to heat release rate), other reaction pathways may lead to significant amount of heat release rate as well at large turbulence intensities (Wang et al. 2018; Wabel et al. 2018). Nonetheless, the DNS of premixed flames is helpful for assessing the capability of the PLIF technique for studying turbulent premixed flames structure and burning rate, see for example the studies of Wang et al. (2018), Haworth et al. (2000), Wabel et al. (2018), Najm et al. (1998).

Although the above briefly reviewed studies are of significant importance as they elaborate the effect of turbulence on premixed flames structure and burning rate, they correspond to compositionally homogeneous mixtures. However, premixed flames may propagate into compositionally inhomogeneous (stratified) fuel–air mixtures in several engineering relevant applications. The stratification is either set through the design of the experimental setups, such as those used in the studies of Sweeney et al. (2011, 2012a, b), Anselmo-Filho et al. (2009), Vena et al. (2015a, b), Seffrin et al. (2010), or it occurs due to turbulent mixing between fuel and air during the fuel injection process, see for example the studies of Galizzi and Escudié (2010), Böhm et al. (2007, 2011), Pasquier et al. (2007), Robin et al. (2008). Nevertheless, stratification can influence the premixed flames topology, reaction layer thickness, as well as the burning rate. Results presented in past investigations (Haworth et al. 2000; Sweeney et al. 2011, 2012a, b; Anselmo-Filho et al. 2009; Vena et al. 2015a, b; Galizzi and Escudié 2010; Böhm et al. 2011; Pasquier et al. 2007) show that, generally, the tested stratified flames feature wrinkled surfaces. This topology is not significantly dependent on the tested turbulence intensities and/or the amount of the stratification (which is the relatively rich fuel–air equivalence ratio divided by the relatively lean fuel–air equivalence ratio). In agreement with the wrinkled flame structure, temperature profile measurements presented in Sweeney et al. (2012a, b) show that the temperature increases from the reactants towards the products featuring an error function-like distribution. Galizzi and Escudié (2010) investigated stratified turbulent V-shaped flames, with one wing of the flame front exposed to lean and one to relatively rich fuel–air mixtures. They Galizzi and Escudié (2010) performed Mie scattering measurements, and their results show that

the flame front features pronounced corrugations on the richer side of the V-flame compared to the leaner side. Nevertheless, the reported corrugations and the flame topology in Galizzi and Escudié (2010) are similar to those of the premixed flames with compositionally homogeneous mixtures at relatively small Karlovitz numbers.

The thickness of the stratified flames have been investigated in the studies of Sweeney et al. (2012a, b), Robin et al. (2008). Results of Robin et al. (2008) suggest, in addition to turbulence, fuel–air equivalence ratio variation (due to stratification) generates excess stretch on the premixed flame surfaces, which causes the thinning of the flames. Compared to Robin et al. (2008), results presented in Sweeney et al. (2012a) suggest that the probability density function of the flame front thickness depends on the swirl number (S, which is defined as the ratio of mean tangential to mean axial velocities in Sweeney et al. (2012a), axial distance from the burner, as well as the amount of stratification. For moderately swirling flames with no stratification, the most probable flame thickness is nearly constant and does not change with increasing the distance from the burner exit plane (Sweeney et al. 2012a). However, for stratified flames, increasing the axial distance from the burner decreases the most probable flame thickness. An opposite behavior is reported in Sweeney et al. (2012a) for highly swirling flames. That is, for stratified conditions, increasing the distance from the burner exit, increases the most probable flame thickness Sweeney et al. (2012a). It is important to highlight that the observation of such behavior may be due to the opposing influences of swirl number on turbulence and stratification. Separating these effects is challenging and requires further investigations.

For stratified flames, Haworth et al. (2000) showed that multiplication of OH and CH_2O mass fractions can be used to visualize the heat release rate regions. They Haworth et al. (2000) visualized that, in addition to the conventional premixed front, a secondary reaction zone may also exist in the products region of the stratified turbulent flames. They Haworth et al. (2000) showed that, for relatively rich conditions, fuel may pass through the main flame region and reignite on the products side provided that enough oxygen is available. The results reported in the literature for the burning rate of the turbulent premixed flames with inhomogeneous mixtures is controversial. Some investigations, such as Haworth et al. (2000), show that stratification does not significantly influence the burning rate (even with the existence of secondary reactions) compared to fully premixed conditions. Similarly, but for a flame displacement-like definition of burning rate, Bonaldo and Kelman (2009) also showed that stratification does not influence the burning rate of the turbulent premixed flames. However, some studies, e.g. (Anselmo-Filho et al. 2009; Zhou et al. 1997; Cho and Santavicca 1993), suggested that stratification increases the flame straining. This leads to generation of more flame surface area, which increases the flame burning rate.

To the best knowledge of the authors, there does not exist a consensus in the literature elaborating effect of stratification on a marker of heat release rate (specifically multiplication of OH and CH_2O PLIF signals) of turbulent premixed flames. The objective of the present study is to investigate how stratification influences this multiplication.

2 Experimental Methodology

The experimental setup, diagnostics, coordinate system, and tested conditions are discussed in this section.

2.1 Setup

The experimental setup is composed of a burner as well as two nozzles that are separately used in the experiments. Details related to these are elaborated below.

Burner: The technical drawing of the burner is shown in Fig. 1. The burner is composed of an air feed section, an expansion section, a settling chamber, a plenum, and an adapter. The air feed section is a hollow cylinder with an inner diameter of 51 mm. Four inlets on the air feed section allow for injection of air into the burner. The air feed section is followed by an expansion section, which has an expansion area ratio of 4. A mesh screen is positioned at the end of the air feed section and at the entrance to the expansion section. The mesh screen is made of stainless steel wires with diameter and spacing of 0.4 and 1 mm, respectively. After the expansion section, a 102 mm long settling chamber is installed. The chamber is equipped with a honeycomb as well as a mesh screen with specifications identical to that used at the entrance to the expansion section as shown in Fig. 1. The mesh screen is positioned 25 mm upstream of the honeycomb. The honeycomb is about 77 mm tall, and each hexagonal cell in the honeycomb has a side length of 3.1 mm. Immediately after the honeycomb and at the entrance to the plenum, one mesh screen with specifications identical to those used upstream is installed. A fuel line that carries mixture of methane and hydrogen is positioned at the centerline of the burner and connects to an injection nozzle at its bottom, see Fig. 1. Hydrogen and methane are well mixed inside a mixing chamber positioned about 5 m upstream of the burner. For confidentiality reasons, details of the fuel/air injection nozzle are not shown

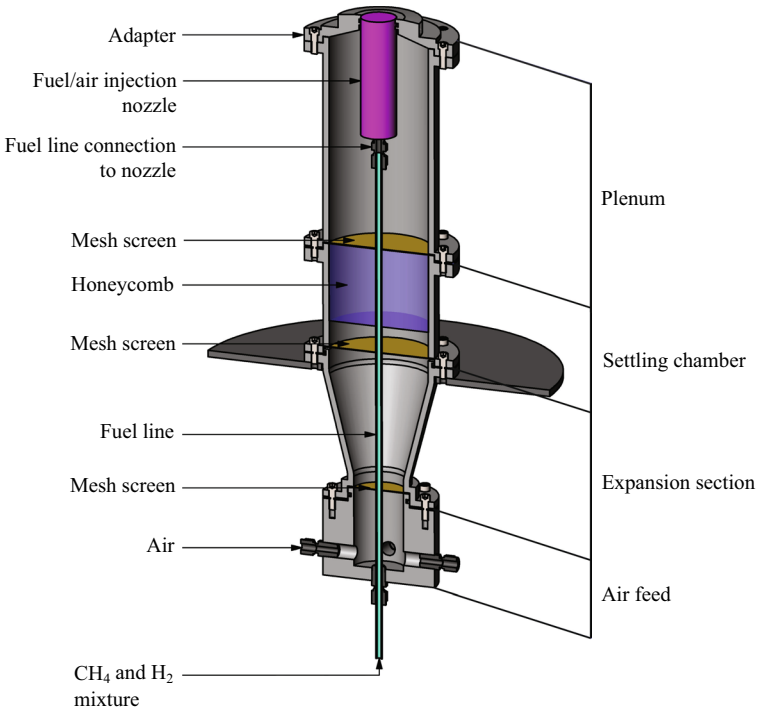

Fig. 1 Technical drawing of the burner

in Fig. 1. However, some nozzle design details are discussed later in this section, then, the corresponding fuel/air mixing characteristics and flow field are thoroughly reviewed in the results section. After air enters the plenum section, it passes through the cylindrical purple surface highlighted as fuel/air injection nozzle in Fig. 1, partially-premixes with the fuel in the nozzle, and then leaves the burner from the exit plane of the nozzle. The adapter, shown in the figure, is a plate that allows for connecting the plenum to the fuel/air injection nozzle.

Nozzles: Two nozzles, referred to as N1 and N2, are utilized in the present investigation. The schematic top view of both nozzles are shown in Fig. 2a, b. In the figure, the shaded region pertains to solid material, and the white region is where the flow exits the nozzles. Both nozzles are composed of 4 symmetrically positioned lobes that carry fuel and air. d is the diameter of the lobes, and s is half of the distance between L1 (L2) and L3 (L4). N2, compared to N1, is designed such that the flow discharged from the nozzle features a swirling motion, which is shown by the dashed circular arrow in Fig. 2b. The fuel line, shown in Fig. 1, that carries mixture of methane and hydrogen is schematically shown by the green dashed-circle at the center of the nozzles in Fig. 2a, b. The fuel flow does not exit at the centerline of the burner. Instead, it flows through several fuel injection holes distributed throughout each lobe, with schematic direction of injection shown in Fig. 2a, b by the green arrows. Due to fuel holes manufacturing tolerances, the total fuel flow rate injected into a given lobe may differ from that of the other lobes. This creates stratification of the fuel–air equivalence ratio, is industrially relevant to gas turbine combustors, and differs from the strategy of stratification used in for example the studies of Sweeney et al. (2011, 2012a, 2012b, 2011), Vena et al. (2015b). Although the size of the fuel injection holes are different, the total injected fuel flow rate inside each lobe and for a given experimental condition is fixed, and as a result, the experiments are repeatable.

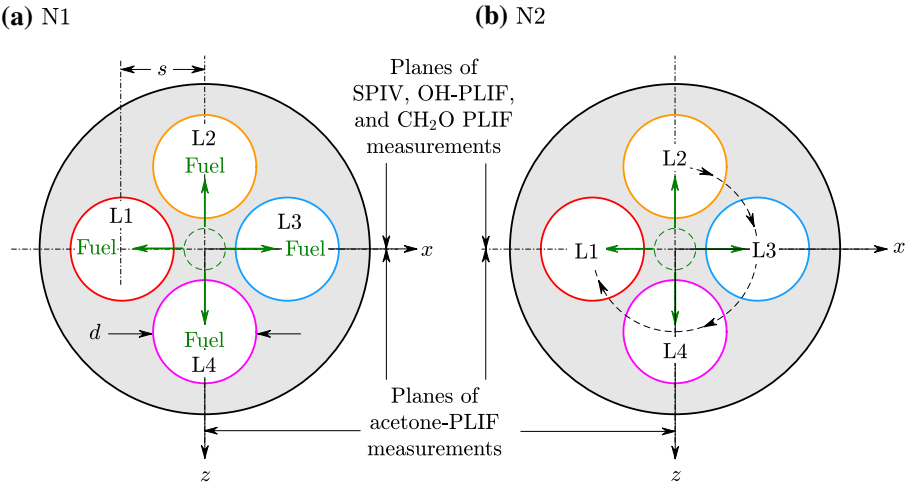

Fig. 2 **a** and **b** are the schematic drawings of nozzles N1 and N2, respectively. L1–L4 are the injection lobes. The direction of salient flow is normal and out of the page. This direction coincides with the y-axis of the coordinate system. The green arrows show the directions of fuel injection into the lobes

2.2 Diagnostics

Simultaneous OH and CH_2O Planar Laser-Induced Fluorescence (PLIF) as well as separate Stereoscopic Particle Image Velocimetry (SPIV) were performed with an acquisition frequency of 1 Hz, similar to Mohammadnejad et al. (2019). Schematics of the diagnostics is shown in Fig. 3. The PLIF excitation system consisted of a two-color Nd:YAG pump laser (Quanta Ray PIV400) and a frequency-doubled dye laser (Sirah Precision Scan). The Quanta Ray laser delivers two laser pulses with wavelengths of 355± 3 nm and 532 nm using a harmonic generator. The 532 nm beam was used to pump the dye laser (see Fig. 3), which excited OH at 282.94 ± 0.005 nm ($Q_1(6)$ line of the (1, 0) vibrational band of the OH A-X system similar to Fayoux et al. (2005), Ayoola et al. (2006, 2009), Hardalupas et al. (2010), Paul and Najm (1998)). The laser beam has a pulse energy and duration of about 11 mJ and 6 ns, respectively. The 355 nm beam was used to excite $CH_2O(\tilde{A}^1A_2 - \tilde{X}^1A_1 4_0^1$ vibronic manifold similar to Fayoux et al. (2005), Hardalupas et al. (2010), Harrington and Smyth (1993), Brackmann et al. (2003), Yamamoto et al. (2011)). The pulse energy and duration of this beam are about 300 mJ and 7 ns, respectively. Both laser beams were formed into collimated and coincident sheets using mirrors (M1–M3) and cylindrical lenses (L1–L3). The sheets pass through the burner centerline, have the thickness of about 250 μm, and span from about 5 to 40 mm above the burner exit plane. The OH and CH_2O PLIF signals were acquired using two PIMAX ICCD cameras. The OH camera was equipped with a Nikon's Nikkor UV lens ($f = 105$ mm, $f\# = 4$) and a bandpass filter with a center wavelength of 320 ± 20 nm. The CH_2O camera was equipped with a Coastal Optics UV lens ($f = 105$ mm, $f\# = 4$) and a longpass filter (Schott GG 395). The projected spatial resolution of the CH_2O and OH images was 89 μm per pixel. The line spread functions of both cameras were acquired using the knife edge technique (see Clemens (2002), Wang and Clemens (2004), and the effective resolution of the optical system

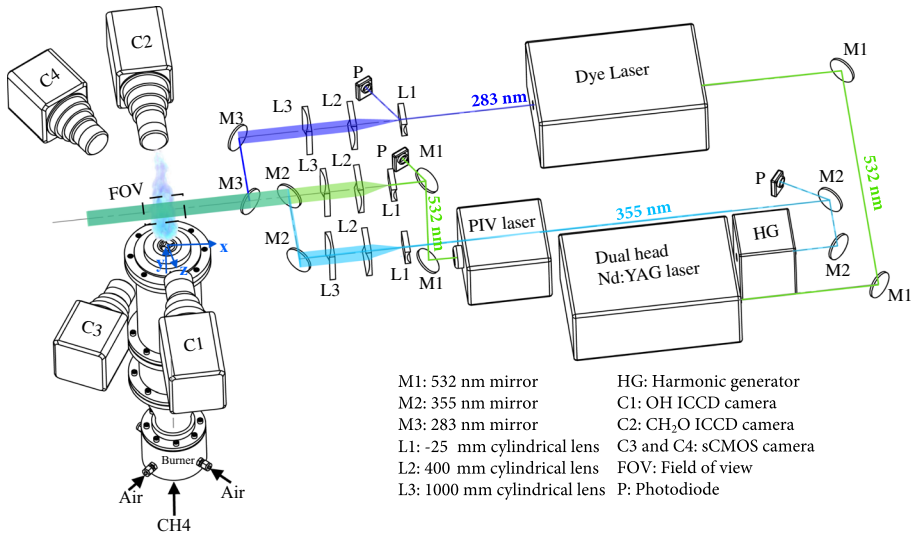

Fig. 3 The diagnostics arrangement. Simultaneous OH-PLIF, CH_2O-PLIF, as well as separate SPIV were performed for reacting conditions. Separate SPIV and acetone-PLIF experiments were performed for non-reacting conditions

(the full width at half maximum of the line-spread function) was estimated to be 263 μm. Further details regarding the PLIF system is provided in Mohammadnejad et al. (2020). The collected OH and CH_2O PLIF images were corrected for the effects of shot-to-shot and spatial variations of the laser pulses, background, and noise following algorithms discussed in the next section. For non-reacting test conditions (discussed in the next subsection), and in order to investigate the distribution of fuel–air equivalence ratio, the 283 nm laser was used for excitation of acetone. For the related experiments, cameras C2, C3, and C4 were turned off, and C1 was equipped with a 305 nm longpass filter. Acetone-PLIF is used in past studies as a fuel tracer for mixtures containing methane (Anselmo-Filho et al. 2009; Weinkauff et al. 2015; Ahmed et al. 2007; Degardin et al. 2006; Elbaz and Roberts 2016) and hydrogen (Yan et al. 2010). However, it is acknowledged that acetone is heavier than methane and hydrogen and has a smaller molecular diffusivity for diffusion into air.

The SPIV system consisted of a dual-cavity, double-pulse, Nd:YAG laser (BSL Twins CFR PIV200) and two sCMOS cameras (LaVision Imager sCMOS) equipped with Scheimpflug adapters and Tokina lenses ($f = 100$ mm, $f\# = 2.8$). The SPIV laser delivers laser pulse pairs at 532 nm, with the separation time between the two pulses being set to either 9 or 47 μs, depending on the tested bulk flow velocity. The laser beam was formed into an approximately 30 mm tall sheet, spanning from about 5 to 35 mm above the burner exit plane. Care was taken to coincide the SPIV laser sheet with those of the PLIF lasers. The flow was seeded with sub-micron size aluminum oxide solid particles using PIVTEC seeder (PIVsolid8). The SPIV cameras (C3 and C4 in Fig. 3) were placed in a forward scatter configuration, with an angle of about 120 degrees between them. The cameras were operated at a frame rate of 1 Hz (frame straddling mode) and imaged a field of view of about 84 mm×70 mm, with a projected spatial resolution of 29.3 μm/pixel. A three-dimensional dot target (LaVision Type 20) was used to map the fields of view from the raw PLIF and SPIV coordinates to the same physical coordinate. In addition to this target plate, an alternative technique was used to assess the accuracy of mapping, with details discussed in Appendix A. It was obtained that the accuracy of mapping was smaller than one pixel. Vector fields were calculated from the spatial cross-correlation using the adaptive evaluation algorithm in a commercial software package (LaVision DaVis 8.4). All measurement equipment was triggered by a LaVision timing unit (PTU X) and an external pulse generator (SRS DG645). The timings of the SPIV laser pulses were detected using DET10A Si-based photodiodes. Timings related to all of the lasers and cameras were monitored using an oscilloscope. To reduce the velocity calculation error, several pre-processing and processing steps were implemented in the PIV software (DaVis 8.4). First, a sliding minimum filter was used to subtract the background. After this, two passes of cross-correlation calculations were performed for vector generation inside 32×32 pixels^2 interrogation windows. Zero overlap between the windows were used, which led to a vector spacing of 0.9 mm. Then, spurious vectors with cross-correlation peak-ratio smaller than 1.5 were removed. Finally, the outlier vectors were detected and removed using a median-based filter (adapted from Westerweel and Scarano 2005) by the PIV software. This procedure for pre-processing and processing of the vector fields is similar to that used in Mohammadnejad et al. (2020).

2.3 Coordinate System

A Cartesian coordinate system (see Figs. 2 and 3), with its origin positioned on the burner centerline and at the exit plane of the nozzle, was used. The x- and y-axes lie within the

imaging field of view (plane of PLIF and SPIV laser sheets). z-axis is normal to the x- and y-axes as well as the imaging filed of view.

2.4 Tested Conditions

Four non-reacting and four reacting conditions are tested, with details tabulated in Table 1. Two mean bulk flow velocities (5 and 25 m/s) for both N1 (non-swirling nozzle) and N2 (swirling nozzle) are examined. The non-reacting conditions are denoted by N1–5–NR, N2–5–NR, N1–25–NR, and N2–25–NR; and, the corresponding reacting conditions are shown by N1–5–R, N2–5–R, N1–25–R, and N2–25–R in the table. For the non-reacting conditions, in addition to the SPIV, acetone-PLIF (denoted by a-PLIF in Table 1) is performed for characterizing the fuel–air equivalence ratio distribution. In the table, L1–L3 and L2–L4 pertain to measurements in the $x-y$ and $y-z$ planes, respectively. The utilized fuel is a mixture of methane and hydrogen. Methane grade 2 and hydrogen grade 5, which are 99% and 99.999% chemically pure, are used in the experiments. The global fuel–air equivalence ratio is 0.8 for all tested conditions. The percentage of hydrogen enrichment, i.e. the ratio of hydrogen volume flow rate to the summation of hydrogen and methane volume flow rates is 60%. For the reacting tests, the fuel (mixture of hydrogen and methane) is injected through the injection holes of the nozzles discussed in Sect. 2.1. This leads to generation of stratified conditions, which are highlighted by the pale green color in Table 1. For the non-reacting experiments, in addition to the stratified conditions, fully premixed conditions were also examined using the acetone-PLIF experiments. For these tests, the fuel line in Fig. 1 was closed, the fuel (mixture of hydrogen and methane) and air were mixed inside a mixing chamber (not shown here), and the mixture was fed into the burner through the air lines of the air feed section in Fig. 1. The mixture then entered the injection nozzle lobes through the purple surface of the nozzle schematically shown in Fig. 1. Then, it left the burner exit plane. These experiments were performed only to facilitate measurement of fuel–air equivalence ratio distribution, which is discussed later in Sect. 4.1.

The characteristics of the background turbulent flow were studied using the SPIV technique for non-reacting flow conditions, with details discussed in Sects. 4.2 and 4.3. These characteristics are summarized in Table 2. In the table, S is the swirl number, and

Table 1 The tested non-reacting (NR) and reacting (R) conditions along with the utilized diagnostics. U_0 is the tested mean bulk flow velocity

Condition	NR/R	U_0	Nozzle	S	FP	a-PLIF	SPIV	OH-PLIF	CH_2O-PLIF
N1–5–NR	NR	5	N1			L1–L3, L2–L4	L1–L3		
N2–5–NR	NR	5	N2			L1–L3, L2–L4	L1–L3		
N1–25–NR	NR	25	N1			L1–L3, L2–L4	L1–L3		
N2–25–NR	NR	25	N2			L1–L3, L2–L4	L1–L3		
N1–5–R	R	5	N1				L1–L3	L1–L3	L1–L3
N2–5–R	R	5	N2				L1–L3	L1–L3	L1–L3
N1–25–R	R	25	N1				L1–L3	L1–L3	L1–L3
N2–25–R	R	25	N2				L1–L3	L1–L3	L1–L3

L1–L3 and L2–L4 pertain to measurements in the $x-y$ and $y-z$ planes, respectively. S and FP stand for the stratified and fully premixed conditions, respectively. (a, OH, and CH_2O)–PLIF pertain to acetone, hydroxyl, and formaldehyde planar laser-induced fluorescence, respectively. SPIV stands for stereoscopic particle image velocimetry

Table 2 Summary of the turbulent flow characteristics

Condition	NR/R	U_0	Nozzle	S	$\overline{u'}$	$\overline{v'}$	$\overline{w'}$	Λ	l_T	η	$\overline{u'}/S_{L0}$	Re_T	Ka	Da
N1–5–NR	NR	5	N1	NA	0.6	0.6	0.6	2.7	0.26	0.08	1.2	108	0.3	14.0
N2–5–NR	NR	5	N2	0.5	0.9	0.9	0.8	2.6	0.21	0.06	1.8	156	0.6	9.0
N1–25–NR	NR	25	N1	NA	2.9	2.8	3.0	2.6	0.11	0.02	5.8	503	3.5	2.8
N2–25–NR	NR	25	N2	0.6	4.4	4.8	4.4	3.3	0.10	0.02	8.8	968	5.7	2.3

For all tested conditions, the fuel–air equivalence ratio, the hydrogen-enrichment percentage, the unstretched laminar flame speed, the laminar flame thickness, and the effective Lewis number are 0.8, 60%, 0.5 m/s, 0.16 mm, and 0.96, respectively. The unit of Λ, l_T, and η is mm. The unit of U_0, $\overline{u'}$, $\overline{v'}$, and $\overline{w'}$ is m/s

is defined by Sweeney et al. (2012a) as the ratio of W (which is the absolute mean velocity along the z-axis) and U (which is the absolute mean velocity along the y-axis) averaged at $y_0 = 5$ mm and $|x| < 20$ mm. N1 does not feature a swirling flow, and as a result, S is not estimated for this nozzle. $\overline{u'}$, $\overline{v'}$, and $\overline{w'}$ are the values of RMS velocity fluctuations spatially averaged at $y_0 = 5$ mm and for $|x| < 20$ mm. Λ is the integral length scale, and is estimated by integrating the autocorrelation of the streamwise velocity data calculated along the y-axis using the formulation presented in Pope (2001) and procedures discussed in Mohammadnejad et al. (2020), Kheirkhah and Gülder (2013). For injector designs that lead to generation and shedding of coherent flow structures, the autocorrelation of the velocity data may feature a nearly periodic spatial variation along the y-axis, which does not allow for calculation of the integral length scale, see Appendix A in Mohammadnejad et al. (2020). In the present study, the autocorrelations do not feature strong coherent fluctuations for $|x| \lesssim 15$ mm. However, for 15 mm $\lesssim |x| \lesssim 20$ mm, coherent flow structures related to the jet shear layers exist. Thus, the integral length scale was spatially averaged over $|x| < 15$ mm and at $y_0 = 5$ mm. The Taylor length scale was estimated using $l_T = \Lambda Re_T^{-1/2}$, with $Re_T = \overline{u'}\Lambda/\nu$ being the turbulent Reynolds number. In the calculation of the turbulent Reynolds number, ν is the reactants kinematic viscosity estimated at 300 K. The Kolmogorov length scale (η) was obtained using $\eta = \Lambda Re_T^{-3/4}$. The Karlovitz and Damköhler numbers were estimated from $Ka = (\overline{u'}/S_{L0})^{3/2}(\Lambda/\delta_l)^{-1/2}$ and $Da = \Lambda S_{L0}/(\delta_l \overline{u'})$. $\delta_l = 0.16$ mm is the laminar flame thickness and is estimated from $\delta_l = \lambda/(\rho_0 c_p S_{L0})$, with λ (thermal conductivity) and c_p (specific heat) estimated at 1500 K, and ρ_0 (reactants density) estimated at 300 K. S_{L0} is the unstretched laminar flame speed and was estimated using Cantera with GRI-Mech 3.0 mechanism Goodwin et al. (2018) for $\phi = 0.8$ and hydrogen-enrichment percentage of 60%. As will be discussed in Sect. 4.1, the tested conditions feature significant variation of the fuel–air equivalence ratio and as a result the unstretched laminar flame speed and thickness. It is important to note that $\overline{u'}/S_{L0}$, Ka, and Da presented in Table 2 correspond to a fully premixed flame. Following the procedures presented in Mohammadnejad et al. (2019), the effective Lewis number was calculated and equals 0.96 for all tested conditions. The formulations used for calculation of the non-dimensional parameters are consistent with those used in the past studies, see for example (Driscoll et al. 2020; Skiba et al. 2018; Mohammadnejad et al. 2020; Peters 2000). Values of the tested non-dimensional parameters suggest N1/N2–5–NR correspond to the corrugated flames, and N1/N2–25–NR correspond to the thin reaction zones regime of the Borghi-Peters diagram (Borghi 1988; Peters 2000). For brevity, the diagram is not presented here.

3 Data Reduction

The procedure for processing the OH-PLIF, CH_2O-PLIF, and their multiplication is discussed in this section. Raw OH and CH_2O PLIF images pertaining to N2–25–R condition are presented in Fig. 4a, b, respectively. First, the background was collected by turning off the PLIF lasers and collecting 500 images using both OH and CH_2O cameras. Background noise refers to the summative effect of flame chemiluminescence and camera sensor electric noise. Background images were averaged and subtracted from the corresponding raw data. Then, two separate sets of experiments (similar to Mohammadnejad et al. 2020) were performed to collect 500 images of the OH and CH_2O laser

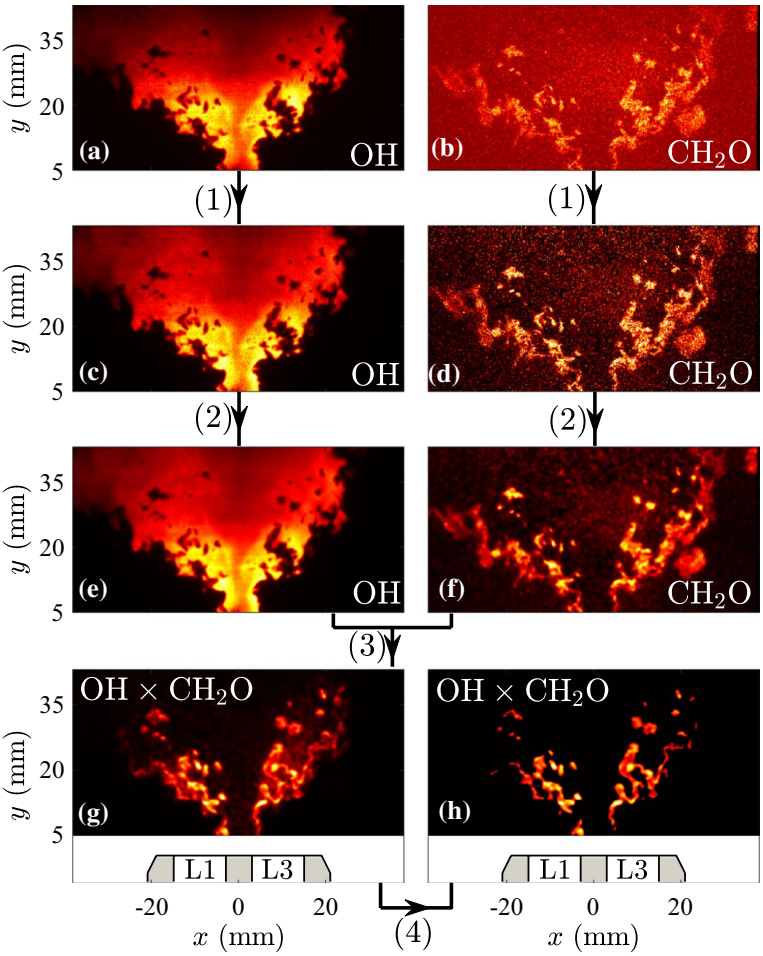

Fig. 4 Procedure of reducing the raw OH and CH_2O PLIF data to that used for the analyses. The results correspond to N2–25–R condition. Process 1 includes background subtraction as well as laser profile energy and shot-to-shot corrections. Process 2 corresponds to median-based filtering. Process 3 is the multiplication of the median-based filtered OH and CH_2O PLIF images, and Process 4 pertains to thresholding $OH_{PLIF} \times CH_2O_{PLIF}$

profiles. These images were averaged to estimate the background for both cameras. Then, the lasers profiles were obtained through separate measurements and were averaged over 500 frames. The background-subtracted images were normalized by the corresponding averaged laser profile as well as the shot-to-shot energy of the lasers collected by photodiodes shown in Fig. 3. The resultant images associated with the OH and CH_2O are shown in Fig. 4c, d, respectively. Next, the images were filtered using 7×7 and 9×9 pixels^2 median-based filters for hydroxyl and formaldehyde data, respectively. The median-based filtered images of OH and formaldehyde PLIF are shown in Fig. 4e, f, respectively. The effect of the median-based filter size on the results is discussed in Appendix B. After median-based filtering, the images were multiplied, with the resultant image shown in Fig. 4g. Finally, a global threshold was applied, with the corresponding results shown in Fig. 4h.

It is important to highlight that the OH and CH_2O PLIF images were not thresholded prior to multiplication. For all tested conditions, 30% of the $OH_{PLIF} \times CH_2O_{PLIF}$ maximum of each image was used for thresholding. This was obtained using a trial and error process. The $OH_{PLIF} \times CH_2O_{PLIF}$ signal for representative frames related to test conditions with smallest (N1–5–R) and largest (N2–25–R) Karlovitz numbers are shown in Fig. 5a, f, respectively. As can be seen, the background noise is present, and as a result, the $OH_{PLIF} \times CH_2O_{PLIF}$ images need to be thresholded. The results in the second to fifth columns pertain to $OH_{PLIF} \times CH_2O_{PLIF}$ thresholded by 10, 20, 30, and 40% of the global maximum of each image, respectively. As can be seen, small values of the threshold (20%) does not allow for removing noise as highlighted by the dashed ellipse in the inset of Fig. 5c. Also, comparison of the insets of Fig. 5d, e shows that excessive thresholding (40%) removes signal, causing generation of holes in the reaction zone as highlighted by the dashed circles in Fig. 5e. Similar results were obtained for the rest of the tested conditions. Thus, the 30% threshold of the global maximum in each $OH_{PLIF} \times CH_2O_{PLIF}$ image was used for thresholding.

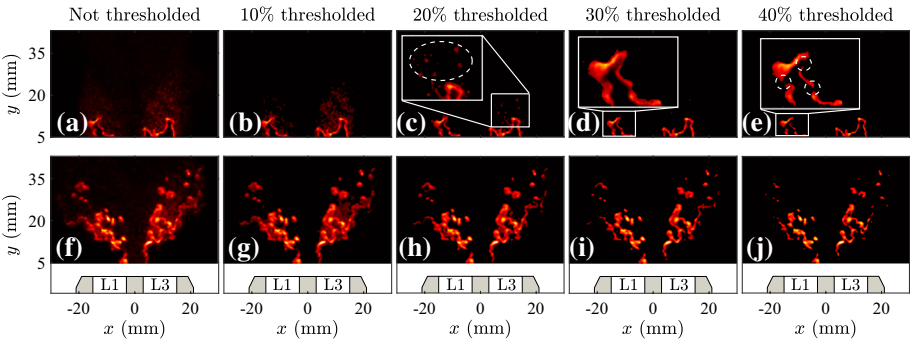

Fig. 5 **a–e** and **f–j** correspond to flames with smallest (N1–5–R) and largest (N2–25–R) tested Karlovitz numbers, respectively. The first column presents $OH_{PLIF} \times CH_2O_{PLIF}$ signals without thresholding. The results in the second to fifth columns pertain to 10, 20, 30, and 40% thresholded $OH_{PLIF} \times CH_2O_{PLIF}$

4 Results

The results are presented in four subsections. In the first subsection, the fuel–air equivalence ratio distribution is estimated, and the amount of stratification is quantified. Then, the time-averaged flow and flame characteristics are presented in the second subsection. In the third subsection, a detailed analysis of the turbulent flow is provided. Finally, in the last subsection, the integral and intensity of $OH_{PLIF} \times CH_2O_{PLIF}$ are estimated, and the effects of the turbulent flow and stratification on these are studied.

4.1 Fuel–Air Equivalence Ratio Distribution

Planar laser-induced fluorescence of acetone was used to study the fuel–air equivalence ratio distribution for non-reacting conditions. A framework that allows for estimation of the fuel–air equivalence ratio distribution is presented here, and the results are discussed afterwards. The ratio of the collected local acetone-PLIF signal to the averaged laser profile (both corrected for the effect of background and shot-to shot laser energy), $S(x,y)/I_{\text{laser}}(x,y)$, is given by Eckbreth (1996) and Kohse-Höinghaus and Jeffries (2002)

$$\frac{S(x,y)}{I_{\text{laser}}(x,y)} = \frac{N(x,y)}{V}\frac{f_B(T)}{Q_{21}(T)}, \tag{1}$$

where $N(x, y)$, f_B, Q_{21}, T, and V are the number of laser-excited acetone molecules, the Boltzmann coefficient, the quenching rate, temperature, and the volume of the region illuminated by the laser sheet, respectively. Dividing and multiplying the RHS of Eq. (1) by the Avogadro's number (N_{AV}), and considering that the number of moles of acetone at an interrogation window with its center positioned at (x, y) is given by $n(x,y) = N(x,y)/N_{AV}$, it can be shown that

$$\frac{S(x,y)}{I_{\text{laser}}(x,y)} = \underbrace{\frac{n(x,y)}{V}}_{[A](x,y)}\frac{f_B(T)}{Q_{21}(T)}N_{AV}, \tag{2}$$

where $[A](x, y)$ is the local concentration of acetone. In Eqs. (1 and 2), the quenching rate generally depends on the local mixture composition as well as temperature, see for example Tamura et al. (1998). Here, it is assumed that the quenching rate only depends on temperature and the dependence on the local mixture composition is neglected. It is acknowledged this assumption may potentially lead to uncertainty in estimation of the local fuel–air equivalence ratio. Calculating the fuel–air equivalence ratio distribution requires a correlation between the concentration of the fuel tracer (i.e. acetone) and the fuel concentration. Here, we assume this correlation is linear. That is $[A](x,y) = k[F](x,y)$, with k being the constant of proportionality and $[F](x, y)$ being the fuel concentration. Using this assumption along with multiplying and dividing RHS of Eq. (2) by the laser illuminated volume, it can be shown that

$$\frac{S(x,y)}{I_{\text{laser}}(x,y)} = kV[F](x,y)\frac{N_{AV}}{V}\frac{f_B(T)}{Q_{21}(T)}. \tag{3}$$

Using the definition of the fuel–air equivalence ratio Turns (1996), $[F](x, y)$, the local concentration of fuel can be obtained from

$$[\mathrm{F}](x,y) = \phi(x,y)\frac{m_{\mathrm{Air}}}{VMW_{\mathrm{F}}}\frac{m_{\mathrm{F}}}{m_{\mathrm{Air}}}|_{\mathrm{st.}}, \tag{4}$$

where m_{Air}, MW_{F}, and m_{F} are the mass of air, molecular weight of the fuel, and mass of the fuel, respectively. $m_{\mathrm{F}}/m_{\mathrm{Air}}|_{\mathrm{st.}}$ is the fuel to air mass ratio estimated at stoichiometric condition. Combining Eqs. (3) and (4) leads to

$$\underbrace{\frac{S(x,y)}{I_{\mathrm{laser}}(x,y)}}_{R(x,y)} = \phi(x,y)\underbrace{\left[\frac{m_{\mathrm{Air}}}{MW_{\mathrm{F}}}\frac{m_{\mathrm{F}}}{m_{\mathrm{Air}}}|_{\mathrm{st}}k\frac{N_{\mathrm{AV}}}{V}\frac{f_{\mathrm{B}}(T)}{Q_{21}(T)}\right]}_{K=\mathrm{constant}}. \tag{5}$$

The Left-Hand-Side (LHS) of Eq. (5) is referred to as $R(x, y)$ and is measured. The multiplier of $\phi(x, y)$, K, is highlighted by the under-brace in Eq. (5) and depends on both temperature and the global fuel–air equivalence ratio. Since the acetone-PLIF experiments are performed for non-reacting conditions (T equals the room temperature and is nearly constant), and that the global fuel–air equivalence ratio is fixed in the present investigation, K is constant. In order to eliminate K in Eq. (5), $R(x, y)$ was measured for both stratified (S) and fully premixed (FP) conditions, which are respectively given by $R(x,y)|_{\mathrm{S}} = K\phi(x,y)|_{\mathrm{S}}$ and $R(x,y)|_{\mathrm{FP}} = K\phi(x,y)|_{\mathrm{FP}}$. Thus, it can be shown that

$$\underbrace{\frac{R(x,y)|_S}{R(x,y)|_{\mathrm{FP}}}}_{r(x,y)} = \frac{\phi(x,y)|_S}{\phi(x,y)|_{\mathrm{FP}}}. \tag{6}$$

Please note that $\phi(x,y)|_{\mathrm{FP}}$ equals the global fuel–air equivalence ratio, i.e. $\phi(x,y)|_{\mathrm{FP}} = 0.8$.

The LHS of Eq. (6), $r(x, y)$, is estimated, time-averaged, and the corresponding results are presented in Fig. 6. The first, second, and third columns of the figure are time-averaged $R(x,y)|_{\mathrm{FP}}$, $R(x,y)|_{\mathrm{S}}$ estimated for L1–L3 ($x-y$ plane), and $R(x,y)|_{\mathrm{S}}$ estimated for L2–L4 ($y-z$ plane), respectively. $R(x,y)|_{\mathrm{FP}}$ is measured for L1–L3, which is similar to that for L2–L4 since the related condition is fully premixed, and all lobes feature similar spatial variation of the acetone PLIF signal. This was confirmed experimentally as well; however, for brevity, the results are not presented here. In Fig. 6, the first through fourth rows pertain to N1–5–NR, N2–5–NR, N1–25–NR, and N2–25–NR test conditions, respectively. The time-averaged values of $r(x, y)$ are presented in the fourth and fifth columns of Fig. 6, respectively. $\bar{r}(x,y) = 1$ means that the time-averaged local fuel–air equivalence ratio equals the global fuel–air equivalence ratio. For regions relatively far from the nozzle center-line, the acetone PLIF intensity is negligible and mixing with room air occurs. These lead to pronounced uncertainty associated with calculation of $\bar{r}$ near the surrounding room air. The regions influenced by this uncertainty ($|x| \gtrsim 15$ mm) are highlighted by the gray color in Fig. 6 and are not used in the calculations. Since the reacting flow experiments are performed in the $x-y$ plane, the variation of $\bar{r}$ estimated at the smallest vertical distance ($y_0 = 5$ mm) and for lobes 1 and 3 were extracted, and the results are shown in Fig. 7.

Comparison of the results related to the non-swirling nozzle (black and red curves) with those of the swirling nozzle (blue and green curves) suggests the trend of the fuel–air equivalence ratio variation along the x-axis and at $y_0 = 5$ mm is nearly independent of the

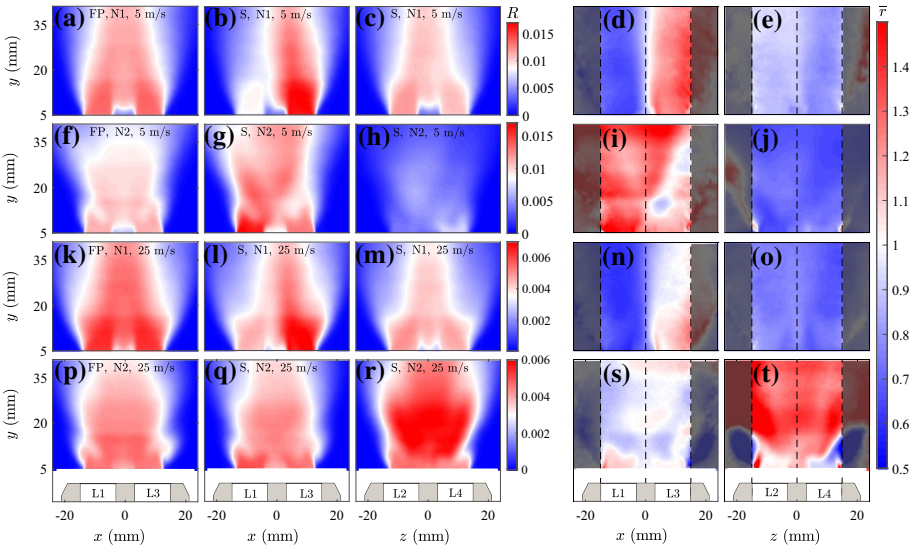

Fig. 6 The first, second, and third columns are the corrected acetone-PLIF signal ($\overline{R}(x, y)$) of the fully premixed mixture, the stratified mixture measured in the $x - y$ plane, and the stratified mixture measured in the $y - z$ plane, respectively. The fourth and fifth columns are the mean of the ratio of the local fuel–air equivalence ratio to the global fuel–air equivalence ratio estimated in the $x - y$ and $y - z$ planes, respectively

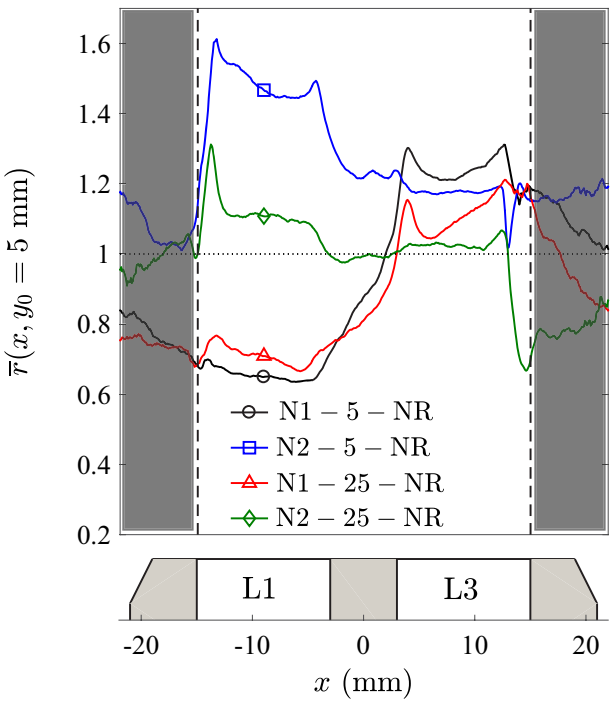

Fig. 7 Values of time-averaged r, see Eq. (6), estimated at $y_0 = 5$ mm and in the $x - y$ plane. In the figure legend, N1 and N2 are the non-swirling and swirling nozzles, respectively

tested mean bulk flow velocity, but it depends strongly on the utilized nozzle. In order to quantify the averaged fuel–air equivalence ratio across a given lobe, $\bar{\bar{r}}$ was estimated using

$$\bar{\bar{r}} = \frac{\int_0^{x_0} \bar{r}(x, y = y_0)\mathrm{d}x}{x_0}, \tag{7}$$

where $y_0 = 5$ mm and x_0 either equals −15 mm or 15 mm, depending on the injection lobe of interest. y_0 is the vertical distance at which the mixture enters the domain of investigation. x_0 is the horizontal distance over which injection takes place, and is highlighted by the dashed lines in Fig. 7. The values of $\bar{\bar{r}}$ estimated for all injection lobes are presented in Table 3. Following Eq. (6), $\bar{\bar{r}} < 1/0.8 = 1.25$ and $\bar{\bar{r}} > 1.25$ correspond to fuel lean and fuel rich conditions, respectively. Results presented in Table 3 show that only lobe 1 of the swirling nozzle (N2) and at 5 m/s carries a slightly rich mixture, with averaged corresponding fuel–air equivalence ratio of $0.8 \times 1.33 = 1.06$. The rest of the lobes and for all tested conditions carry lean mixtures. As can be seen, for the non-swirling nozzle (N1) and for both tested mean bulk flow velocities, while both lobes feature a lean mixture, lobe 3 carries more fuel compared to lobe 1.

Since all the fuel supplied to the injector passes through L1–L4, the averaged fuel–air equivalence ratio estimated from the above framework should equate to the tested global fuel–air equivalence ratio (0.8). Similarly, values of $\bar{\bar{r}}$ averaged for all four lobes should equate to unity. To assess this, the values of $\bar{\bar{r}}$ averaged for all four lobes were calculated and the results are presented in the eighth column of Table 3. As can be seen, the values are close to unity. This suggests that the utilized method for calculation of the fuel–air equivalence ratio distribution is reliable. Despite the values of $\bar{\bar{r}}$ averaged for all lobes being close to unity, deviations from unity are observed which can be attributed to two sources of error. The first source of error is related to the assumptions that the quenching rate is independent of the local mixture composition and that the fuel concentration is proportional to the acetone concentration, which were made to obtain Eq. (3). The second source of error is related to the variability of the laser energy used for acetone excitation. Although the total as well as the spatial variation of the acetone-PLIF laser energy were measured and used for normalization of the results, the variability of these signals near their corresponding mean values leads to error in calculation of the fuel–air equivalence ratio distribution. Analysis of the results shows that $\overline{R}(x, y_0 = 5\ \mathrm{mm})$ varies between 8 to 10%. This last source of error is expected to contribute to the small deviations from unity for $\sum \bar{\bar{r}}_{\mathrm{L}i}/4$ presented in Table 3.

In order to quantify the relative amount of the fuel–air equivalence ratio stratification, two parameters are utilized, which are

Table 3 The time and spatially averaged fuel–air equivalence ratio measured at each lobe divided by the global fuel–air equivalence ratio ($\bar{r}$)

Condition	Nozzle	U_0 (m/s)	$\bar{\bar{r}}_{\mathrm{L1}}$	$\bar{\bar{r}}_{\mathrm{L3}}$	$\bar{\bar{r}}_{\mathrm{L2}}$	$\bar{\bar{r}}_{\mathrm{L4}}$	$\sum \bar{\bar{r}}_{\mathrm{L}i}/4$	σ_{13}	σ_{24}	$\lvert\sigma_{13}\rvert + \lvert\sigma_{24}\rvert$
N1–5–NR	N1	5	0.70	1.17	0.87	0.82	0.89	− 0.50	0.06	0.56
N2–5–NR	N2	5	1.33	1.18	0.52	0.69	0.93	0.12	− 0.28	0.40
N1–25–NR	N1	25	0.73	1.06	0.79	0.74	0.83	− 0.37	0.06	0.43
N2–25–NR	N2	25	1.07	0.93	1.10	0.95	1.01	0.14	0.15	0.29

σ_{13} and σ_{24} are given in Eq. (8). L1, L2, L3, and L4 refer to fuel/air injection lobes 1–4, respectively

$$\sigma_{13} = \frac{\bar{\bar{r}}_{L1} - \bar{\bar{r}}_{L3}}{\frac{1}{2}(\bar{\bar{r}}_{L1} + \bar{\bar{r}}_{L3})}, \tag{8a}$$

$$\sigma_{24} = \frac{\bar{\bar{r}}_{L2} - \bar{\bar{r}}_{L4}}{\frac{1}{2}(\bar{\bar{r}}_{L2} + \bar{\bar{r}}_{L4})}. \tag{8b}$$

Positive (negative) values of σ_{13} mean that lobe 1 injects fuel–air mixture that is richer (leaner) than that of lobe 1. Large absolute values of σ_{13} and σ_{24} mean there exists a strong stratification between the lobes. As can be seen, for lobes 1 and 3, the amount of stratification generated by the non-swirling nozzle is more than that for the swirling nozzle. In order to quantify the overall amount of stratification, the values of $|\sigma_{13}| + |\sigma_{24}|$ were estimated and the results are presented in the last column of Table 3. Small values of $|\sigma_{13}| + |\sigma_{24}|$ suggest better mixing of fuel and air. As can be seen, for both tested mean bulk flow velocities, the swirling nozzle generates the most homogeneous mixture. For both nozzles, the homogeneity of mixture generally increases with increasing the mean bulk flow velocity.

4.2 Time-Averaged Flow and Flame Characteristics

Spatial variation of the mean velocity components along y (U), x (V), and z (W) directions are presented in Fig. 8. The uncertainties associated with estimation of U, V, and W are provided in Appendix C. The results in Fig. 8 correspond to the $x - y$ plane which passes through lobes 1 and 3. The first (second) and third (fourth) rows are associated with the non-reacting (reacting) conditions. The first and second as well as the third and fourth rows pertain to mean bulk flow velocities of 5 and 25 m/s, respectively. The non-reacting flow mean velocity fields of the non-swirlng nozzle show that, for both tested mean bulk flow velocities, there exists a bluff body wake recirculation zone between lobes 1 and 3. This is illustrated by the mean flow streamlines and mean velocity vectors in Fig. 9. In the figure, approximate boundary of the recirculation zone is shown by the contour of $U = 0$, see the red curve near $x = 0$ inside the green color ellipses in Fig. 9a, b. As can be seen, for the

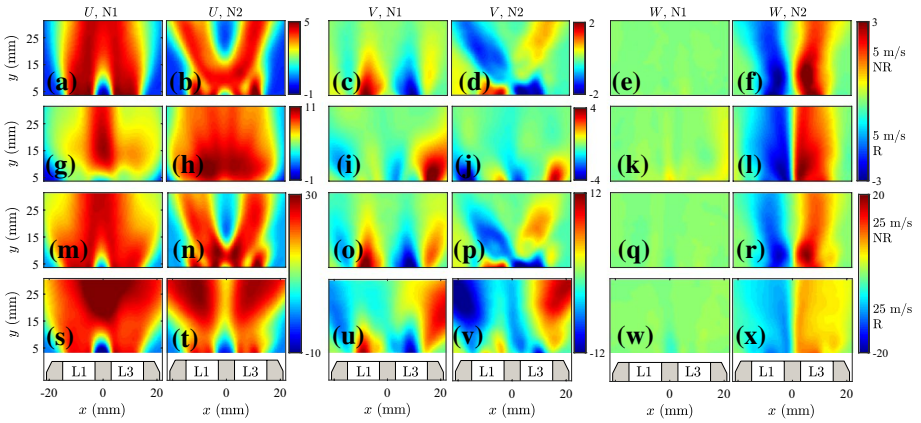

Fig. 8 Time-averaged velocity components along y (first and second columns), x (third and fourth columns), and z (fifth and sixth columns) directions

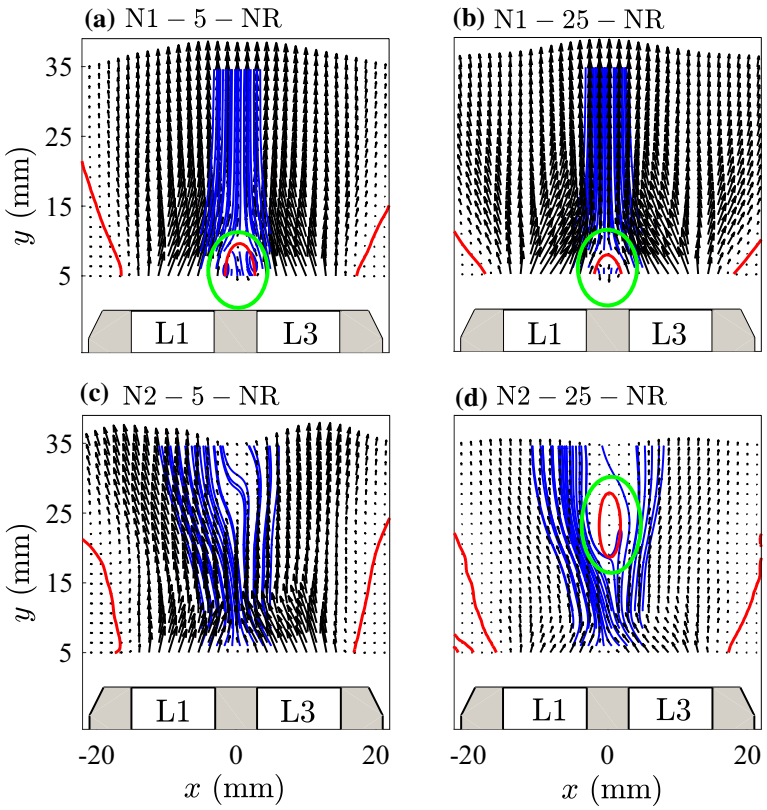

Fig. 9 Time-averaged velocity vector fields for non-reacting conditions. The red curves highlight the loci of $U = 0$, and the green color ellipses highlight the regions related to both bluff body recirculation and vortex breakdown bubbles

non-reacting condition and for the non-swirling nozzle, the size of the recirculation bubble decreases with increasing the mean bulk flow velocity.

For the non-swirling nozzle and for non-reacting flow conditions, the results presented in Fig. 8c, o as well as Fig. 8e, q show that the mean transverse velocity, V, changes sign across the jet shear layers; and, the mean of the velocity normal to the plane of measurements is negligible. Compared to the non-swirling nozzle, N2 generates a swirling motion, which is evident in Fig. 8f, r by the change of W sign along the x direction. For the swirling nozzle, the bluff body recirculation bubble does not exist in the domain of investigation. Instead, a recirculation zone, referred to as vortex breakdown bubble (O'Connor and Lieuwen 2012; Sheen et al. 1996; Huang and Yang 2005), is formed farther downstream and near $y = 20 - 26$ mm for mean bulk flow velocity of 25 m/s, see Fig. 9d. For N2 and at 5 m/s, although the in-plane velocity magnitude is significantly decreased along the vertical axis (see Fig. 9c), the vortex breakdown bubble does not exist for this condition.

In order to elaborate the mean velocity fields of the reacting conditions, sample instantaneous fields of OH, CH_2O, and $OH \times CH_2O$ are presented in the first, second, and third columns of Fig. 10, respectively. The first through fourth rows pertain to N1–5–R, N2–5–R, N1–25–R, and N2–25–R test conditions, respectively. The

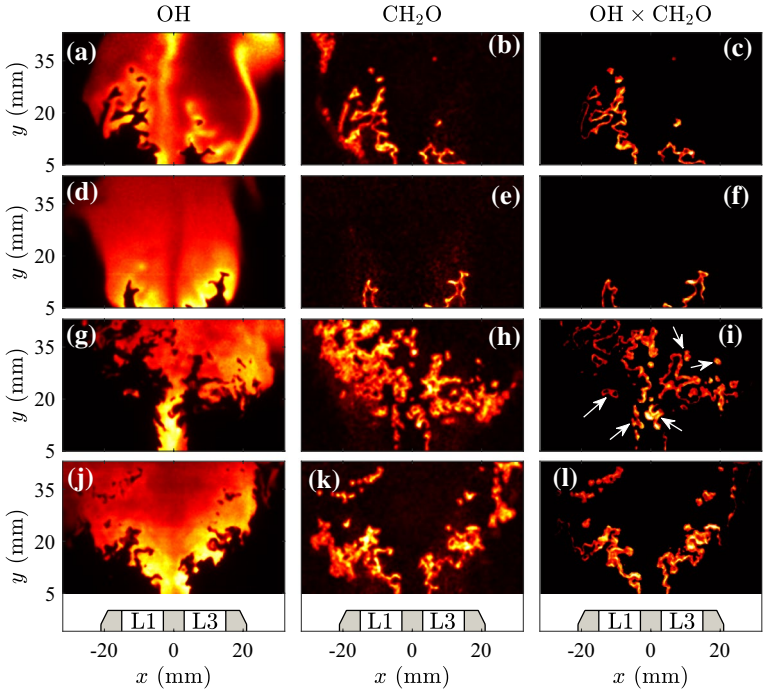

Fig. 10 Representative OH PLIF (first column), CH_2O PLIF (second column), and $OH \times CH_2O$ (third column). The first through fourth rows pertain to N1–5–R, N2–5–R, N1–25–R, and N2–25–R test conditions

time-averaged values of the above parameters are presented in Fig. 11. Please note that the maximum and minimum of the contour presentations in Figs. 10 and 11 are individually set for clarity purposes. As can be seen, for the non-swirling nozzle and at 5 m/s, the flame associated with lobe 3 is a Bunsen-type flame, and that associated with lobe 1 is detached on the left-hand-side. Flames related to N2–5–R are attached on both sides, but those of N1–25–R and N2–25–R are only attached close to $x = 0$. The detachment of the flames pertaining to the non-swirling nozzle and on the left-hand-side is related to the relatively small fuel–air equivalence ratio related to lobe 1, see Table 3.

For both N1 and N2 and for the reacting conditions related to mean bulk flow velocity of 25 m/s, a bluff body recirculation zone near the burner exit and around $x = 0$ is formed, which is highlighted by the green color ellipses shown in Fig. 12b, d. These recirculation zones contain combustion products (see large values of OH PLIF in Fig. 10g, j as well as Fig. 11g, j near $x = 0$), which anchor the flame. Compared to flames generated at the larger mean bulk flow velocity (25 m/s), those generated by the swirling nozzle and at 5 m/s (N2–5–R) are anchored at the exit of the lobes, and as a result, the corresponding flame height is relatively short. Similarly, flames of N1–5–R associated with L3 are anchored at this lobe. The relatively short flame heights of N2–5–R on both sides as well as the right-hand-side (RHS) of N1–5–R and N1–25–R are associated with the large values of the fuel–air equivalence ratio leaving the related lobes (see the related values of $\bar{r}$ in Table 3).

The results presented in Fig. 11a show two regions of relatively large OH PLIF signal, which are highlighted by the dashed boxes. These regions are associated with the

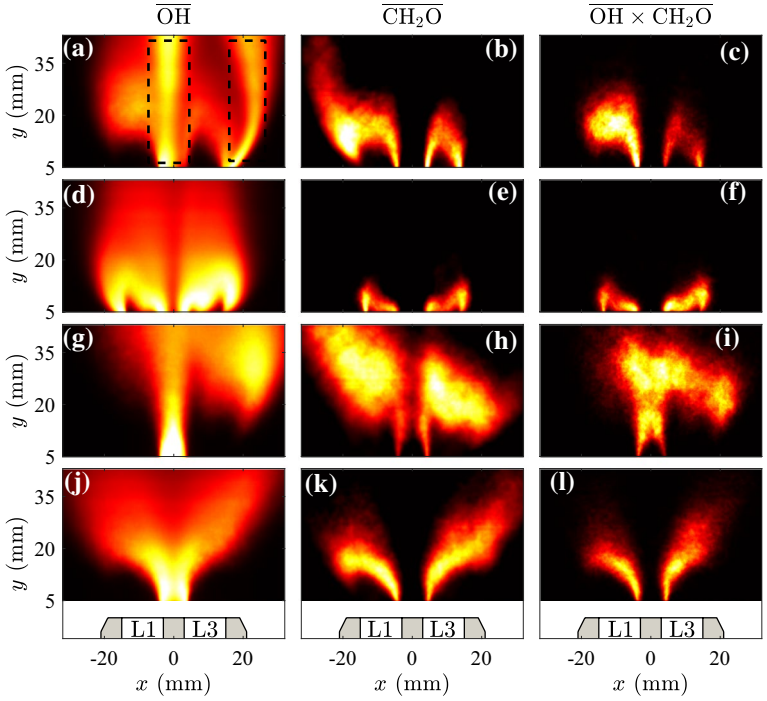

Fig. 11 Time-averaged OH PLIF (first column), CH_2O PLIF (second column), and $OH \times CH_2O$ (third column) data. The first through fourth rows pertain to N1–5–R, N2–5–R, N1–25–R, and N2–25–R test conditions, respectively

relatively rich mixture that leaves lobe 3 of the non-swirling nozzle tested at the mean bulk flow velocity of 5 m/s, see $\overline{\bar{r}}_{L3}$ for this condition in Table 1. Although the amount of time-averaged OH PLIF signal is relatively large inside the boxes shown in Fig. 11a, the corresponding formaldehyde signal is negligible, leading to nearly zero $\overline{OH \times CH_2O}$.

4.3 Turbulent Flow Characteristics

A detailed analysis of the turbulent flow is performed and the results are presented in this subsection. The RMS velocity fluctuations pertaining to the conditions presented in Fig. 8 are shown in Fig. 13. The first and second, third and fourth, as well as fifth and sixth columns present RMS velocity fluctuations along the y, x, and z-axes, respectively. The uncertainty related to estimation of these parameters are provided in Appendix C. The first (second) and third (fourth) rows pertain to mean bulk flow velocities of 5 and 25 m/s for non-reacting (reacting) conditions, respectively. The RMS velocities of the non-reacting flow are relatively pronounced in the regions highlighted by the dashed-boxes in Fig. 13. The interaction of the jets leaving lobes 1 and 3 with the surrounding quiescent air as well as the decelerated flow regions shown in Fig. 8 generate the large RMS velocity fluctuations presented in Fig. 13a–f and m–r. For instance, the large RMS velocity regions highlighted by the magenta color dashed boxes at the center as well as the periphery of the jets in Fig. 13a, c are associated with the jet-jet and jet-surrounding air interactions, respectively. The V-shaped regions with the large RMS velocity shown

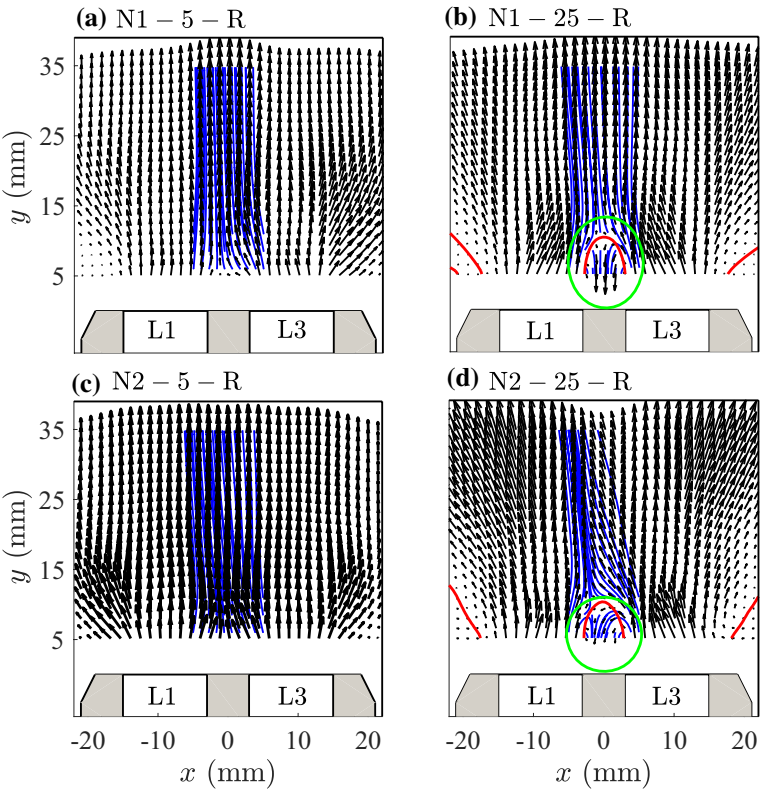

Fig. 12 Time-averaged velocity vector for reacting conditions. The blue curves are the mean flow streamlines. The red curves highlight loci of $U = 0$, and the green color ellipses highlight the recirculation bubbles

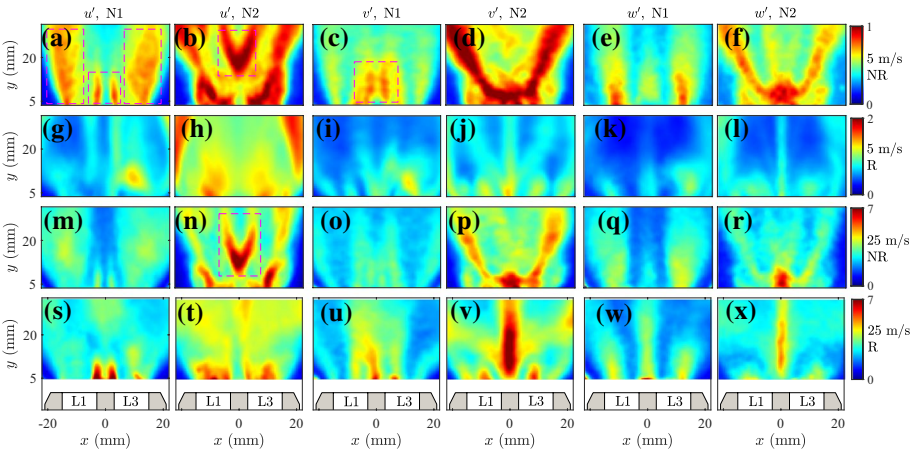

Fig. 13 Root mean square of the velocity fluctuations along y (first and second columns), x (third and fourth columns), and z (fifth and sixth columns) axes

in Fig. 13b, n are generated due to the interaction between the jets that leave lobes 1 and 3 of N2 and the central low velocity region shown in Fig. 8b, n. Since the small mean velocity regions associated with the surrounding air and the recirculation bubbles are mitigated after the burner is lit, the RMS velocity fluctuations become less pronounced for the reacting conditions and in these regions.

For comparison purposes, the values of RMS velocity fluctuations at $y_0 = 5$ mm were extracted from the results shown in Fig. 13 and are presented in Fig. 14a, b, which correspond to reacting and non-reacting conditions, respectively. Variations with black, blue, red, and green colors pertain to N1–5–NR/R, N2–5–NR/R, N1–25–NR/R, and N2–25–NR/R, respectively. The results associated with the solid, dashed, and dotted dashed colors pertain to velocity fluctuations along y-, x-, and z-axes, respectively. The values of these parameters were averaged along the x-axis and at $y_0 = 5$ mm, and the averaged results were presented in Table 2. As can be seen, the background RMS fluctuations for both swirling and non-swirling nozzles are very similar at mean bulk flow velocity of 5 m/s. However, at 25 m/s, the RMS velocity fluctuations are larger for the swirling nozzle compared to the non-swirling nozzle. The above discussions suggest that, compared to the non-swirling nozzle, the swirling nozzle generates relatively large RMS velocity fluctuations at mean bulk flow velocity of 25 m/s. Although such information is important, it does not allow for elaborating some characteristics related to stratified turbulent flames. For example, the results presented in Fig. 10i show that $OH_{PLIF} \times CH_2O_{PLIF}$ may be fragmented and pockets can be formed, as shown by the white arrows in the figure. It is speculated that, in addition to stratification, the local kinetic energy of turbulent eddies may be linked to generation of such flame structures. Thus, in addition to RMS velocity fluctuations presented in Fig. 13, parameters that account for kinetic energy of the eddies should be used to understand how stratified reaction zones interact with turbulence. In order to investigate this, the energetic eddies are detected, and their rotational kinetic energy is estimated. Such analysis is necessary for studying the combined effect of turbulence and stratification on $OH_{PLIF} \times CH_2O_{PLIF}$ signal of the tested flames.

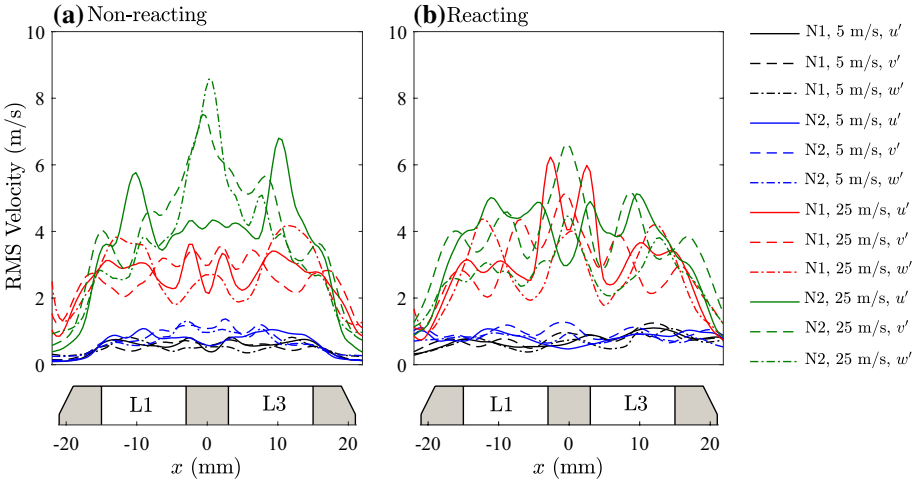

Fig. 14 RMS velocity fluctuations at $y_0 = 5$ mm

The Q-criterion is used for detection of the turbulent eddies (Jeong and Hussain 1995; Cucitore et al. 1999). For all test conditions, the values of Q were estimated using

$$Q = -\frac{1}{2}\left[\left(\frac{\partial u}{\partial y}\right)^2 + 2\frac{\partial u}{\partial x}\frac{\partial v}{\partial y} + \left(\frac{\partial v}{\partial x}\right)^2\right]. \tag{9}$$

Positive values of Q pertain to regions where the swirling strength of the eddies dominate the strain rate. A representative Q field for a given frame of N1–25–R condition is shown in Fig. 15a. The uncertainty associated with estimation of Q is provided in Appendix C. The corresponding rotational speed raised to the power of two, $\zeta^2 = [\frac{1}{2}(\frac{\partial v}{\partial y} - \frac{\partial u}{\partial x})]^2$, was estimated and the results are shown in Fig. 15b. A representative eddy detected by the Q-criterion at $y = 33$ mm is highlighted in Fig. 15a, and the corresponding ζ^2 is shown in Fig. 15b. This eddy can be detected using both the Q-criterion and ζ^2. However, the region shown by the dashed circle at $y = 28$ mm in Fig. 15a features a nearly zero value of Q, but the corresponding ζ^2 is non-zero. This is due to the highlighted region featuring significant contribution from flow straining instead of the swirling motion. The swirling motion significantly influences the turbulence and flame interaction, see Mohammadnejad et al. (2020), and is used for the analyses presented here.

The specific (normalized by mass) turbulent kinetic energy of an eddy can be estimated from Mohammadnejad et al. (2020)

$$T = \sum_{i=1}^{n_e} \frac{1}{2}(r_i\zeta_i)^2, \tag{10}$$

where the index i corresponds to the i^{th} interrogation window inside a given detected eddy. n_e is the number of interrogation windows forming an eddy. r_i is the distance between the center of the i^{th} interrogation window and the center of area of the detected eddy. Following the definitions provided in Jeong and Hussain (1995), it can be shown that

$$\zeta_i^2 = Q_i + \frac{1}{2}||S||_i^2, \tag{11}$$

where $||S||_i$ is the trace of the strain rate matrix calculated at the i^{th} interrogation window. Combining Eqs. (10) and (11), it can be shown that

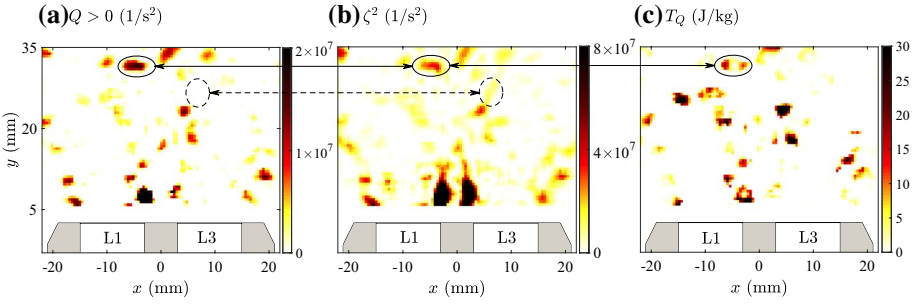

Fig. 15 **a** is a representative and instantaneous Q field. **b** is the vorticity field raised to the power of two related to the results shown in (**a**). **c** is the portion of the eddy kinetic energy due to the swirling motion. The results in **c** correspond to the same instant presented in (**a**, **b**). The results pertain to N1–25–R condition

$$T = \sum_{i=1}^{n_e} \underbrace{\frac{1}{2} r_i^2 Q_i}_{T_Q(i)} + \sum_{i=1}^{n_e} \underbrace{\frac{1}{4} r_i^2 ||S||_i^2}_{T_S(i)}. \tag{12}$$

The first and second terms on the RHS of Eq. (12) pertain to the swirling strength and strain rate of an eddy, respectively. For the representative frame and test condition presented in Fig. 15a, the turbulent eddies are detected (using $Q > 0$ criterion), and values of T_Q are estimated and shown in Fig. 15c. For each test condition, the swirling strength of an eddy, $\sum_{i=1}^{n_e} T_Q(i)$, was estimated for all collected frames, the corresponding PDFs were calculated, and the results are shown in Fig. 16. The results in Fig. 16a, b pertain to non-reacting and reacting conditions, respectively; and, the PDFs are normalized by the corresponding maximum values. As can be seen, for both non-reacting and reacting conditions, increasing the mean bulk flow velocity increases the possibility of existence of eddies with a given specific kinetic energy due to the eddy swirling motion. The results show that, for non-reacting conditions, flow field of the swirling nozzle features large possibilities of eddies for all values of the swirling strength. For reacting conditions and at 5 m/s, $\sum_{i=1}^{n_e} T_Q(i)$ PDF distribution is similar for both nozzles. However, at 25 m/s, the swirling nozzle features large possibilities of eddies at a given swirling strength compared to that for the non-swirling nozzle, which is similar to the observation made for non-reacting conditions. This means, generally, the swirling nozzle is more effective in generating eddies with greater T_Q values. Thus, for homogeneous mixtures, it can be expected that the swirling nozzle generates faster burning flames compared to the non-swirling nozzle and at 25 m/s. However, stratification can potentially alter this conclusion, which is discussed in detail in Sect. 4.4.

Although the above discussion allows to elaborate the probability of generating eddies with a given swirling strength, for different tested nozzles, it does not allow to assess which regions of the flow contribute to generation of large T_Q. The values of T_Q were calculated for all 500 frames of each condition, and the time-averaged results are presented in Figs. 17 and 18, corresponding to mean bulk flow velocities of 5 and 25 m/s, respectively. The uncertainty related to calculation of T_Q is provided in Appendix

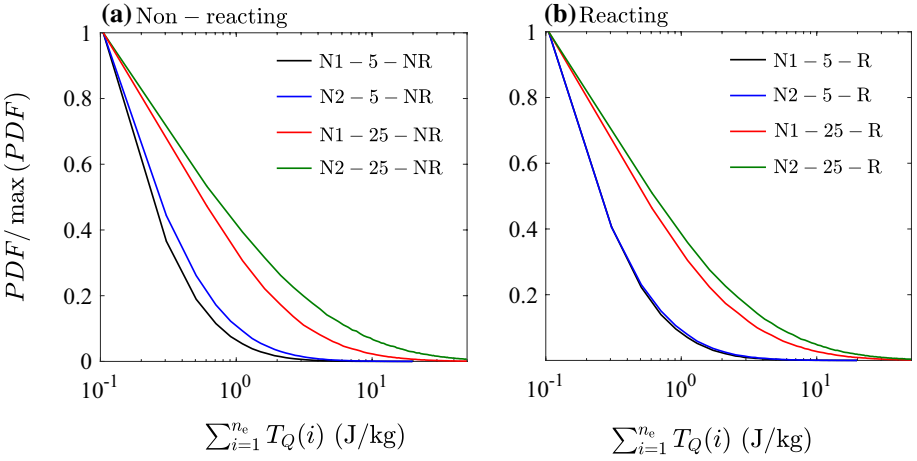

Fig. 16 The normalized probability density functions of T_Q for **a** non-reacting and **b** reacting conditions

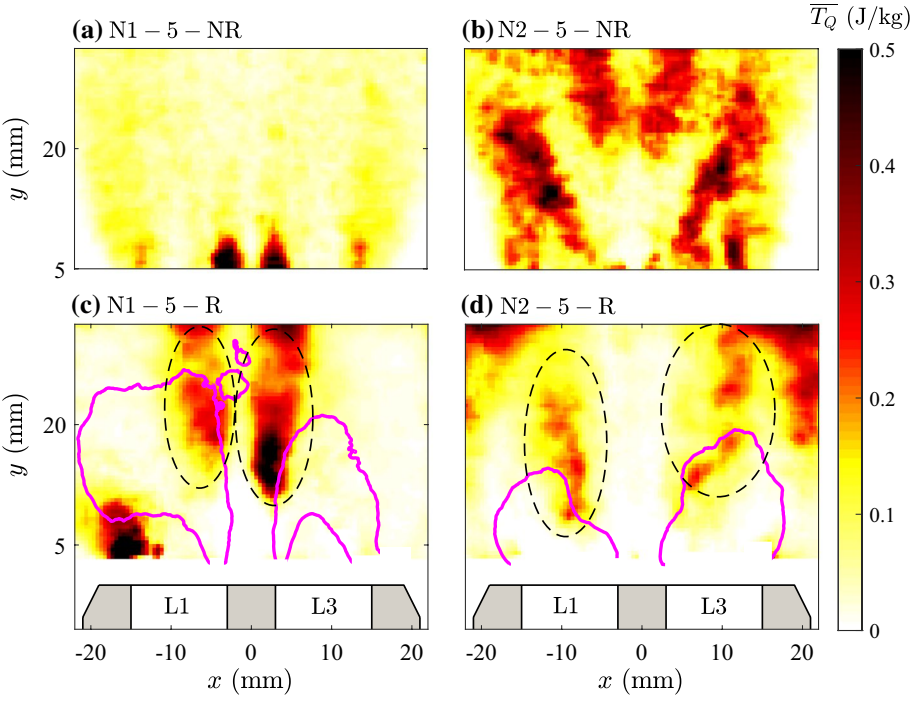

Fig. 17 Mean of the portion of eddy kinetic energy due to swirling motion. The first and second columns pertain to nozzles N1 and N2, respectively. The mean bulk flow velocity is 5 m/s

C. In Figs. 17 and 18, the first and second rows pertain to non-reacting and reacting conditions, respectively. The first and second columns pertain to the non-swirling and swirling nozzles, respectively. For comparison purposes, contours pertaining to 20% of the global maximum of $\overline{\mathrm{OH} \times \mathrm{CH_2O}}$ are also overlaid on Fig. 17c, d as well as on Fig. 18c, d by the magenta color curves. As can be seen, there exist regions downstream of the flames that feature relatively large values of $\overline{T_Q}$. These regions are highlighted by the black dashed ellipses in Fig. 17c, d as well as Fig. 18c, d. This result show that the investigated flames can generate eddies with relatively large values of $\overline{T_Q}$ in the post-flame region. As a result, the PDFs presented in Fig. 16b feature contributions from flame generated turbulence. For comparison purposes, the variation of $\overline{T_Q}$ at $y_0 = 5$ mm is presented in Fig. 19. As can be seen, for both tested mean bulk flow velocities, $\overline{T_Q}$ near lobes 1 and 3 is relatively larger for the swirling nozzle compared to the non-swirling nozzle, especially at 25 m/s and for the non-reacting condition.

In essence, the above discussions suggest that, for the tested conditions and flow/flame geometries of the present investigation, both RMS velocity calculations as well as the kinetic energy associated with the swirling motion of the eddies (which are expected to influence the flame structure and the multiplication of the OH and formaldehyde PLIF signals) are relatively large for the swirling nozzle compared to the non-swirling nozzle especially at the mean bulk flow velocity of 25 m/s.

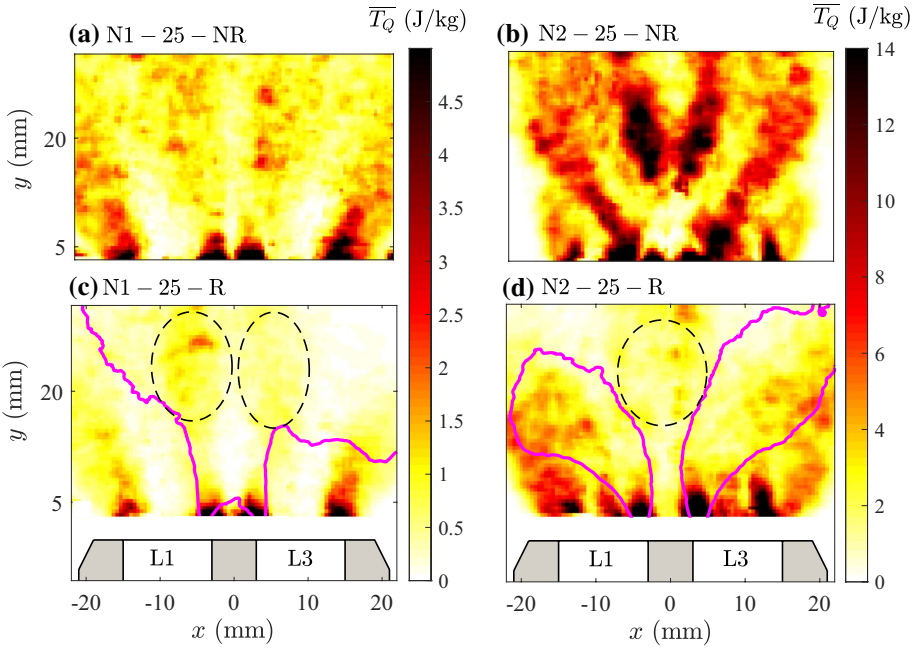

Fig. 18 Mean of the portion of eddy kinetic energy due to swirling motion. The first and second columns pertain to nozzles N1 and N2, respectively. The mean bulk flow velocity is 25 m/s

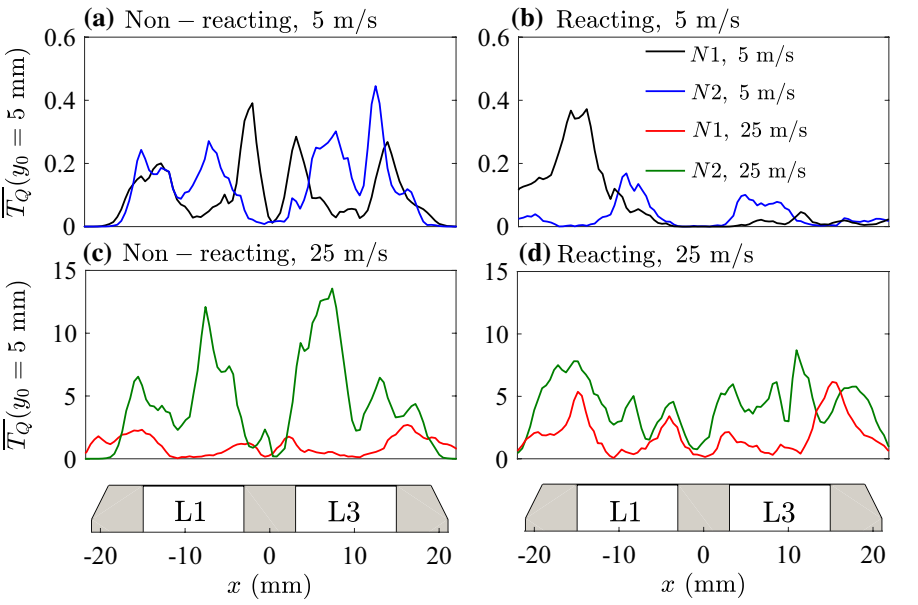

Fig. 19 **a** and **c** as well as **b** and **d** are the time-averaged values of T_Q estimated at $y_0 = 5$ mm for non-reacting and reacting conditions, respectively. **a**, **b** as well as **c** and **d** pertain to mean bulk flow velocities of 5 and 25 m/s

4.4 $OH_{PLIF} \times CH_2O_{PLIF}$ of Stratified Turbulent Flames

Multiplication of OH and CH_2O PLIF signals has been used to mark/visualize the heat release rate of fully and stratified flames for mixtures of air and fuel such as methane (Wabel et al. 2018; Najm et al. 1998), hydrogen-enriched methane (Mohammadnejad et al. 2019), ethylene (Ayoola et al. 2006), propane (Fayoux et al. 2005), and iso-octane (Vena et al. 2015a) in the past. Similarly, the multiplication of the OH and CH_2O PLIF signals is used here for studying hydrogen-enriched methane–air flames. It is important to note that the relation between the OH and CH_2O PLIF multiplication and the true heat release rate can be influenced by several factors including the imaging resolution, the turbulence intensity, and the amount of stratification. The presented results do not provide information related to the true heat release rate and/or burning rate. Here, the effect of stratification on the multiplication of OH and CH_2O PLIF signals is studied.

The double integral of $OH_{PLIF} \times CH_2O_{PLIF}$ normalized by the domain of investigation area ($\Delta x \Delta y$) is estimated for each frame and for all tested conditions. The probability density function of this parameter is presented in Fig. 20. The results presented in the figure can be generally influenced by lack of accuracy in registration of the PLIF signals, the threshold value used for analysis of $OH_{PLIF} \times CH_2O_{PLIF}$, as well as the size of the median-based filters used for reduction of the PLIF signals. The effects of these parameters on $OH_{PLIF} \times CH_2O_{PLIF}$ integral are discussed in Appendix B. For mean bulk flow velocity of 5 m/s, the most probable value of the $OH_{PLIF} \times CH_2O_{PLIF}$ integral is larger by about 7% for the swirling nozzle compared to the non-swirling nozzle. Note that, while the value of $\overline{\overline{r}}$ is approximately the same for lobe 3 and for both N1–5–NR and N2–5–NR conditions, that for lobe 1 and for the N2–5–NR condition is about 47% larger than that for N1–5–NR. $\overline{\overline{r}}$ near lobe 1 is 1.33 for N2–5–NR compared to 0.7 for N1–5–NR condition, see Table 3. Cantera simulations (with GRI-Mech 3.0) was performed to estimate the laminar flame speed of a freely propagating premixed flame of methane and hydrogen with 60% hydrogen-enrichment and for fuel–air equivalence ratios of $0.7 \times 0.8 \approx 0.6$ and $1.33 \times 0.8 \approx 1.1$. The laminar flame speeds for fuel–air equivalence ratios of 0.6 and 1.1 are about 0.23 and 0.73 m/s, respectively. This means that the laminar premixed flame speed corresponding to lobe 1 and for the swirling nozzle is about 68% larger than that for the non-swirling nozzle. Thus, the larger integral of $OH_{PLIF} \times CH_2O_{PLIF}$ for the swirling nozzle compared to the

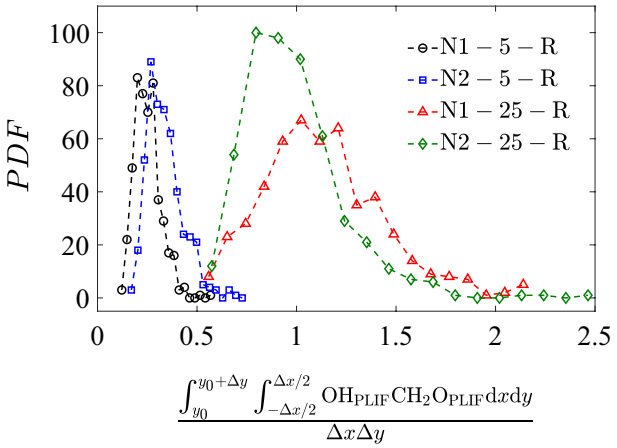

Fig. 20 The probability density function of $OH_{PLIF} \times CH_2O_{PLIF}$ integral

non-swirling nozzle can be due to the large laminar flame speed of relatively rich mixture that leaves lobe 1 of the swirling nozzle.

In contrast with the results related to the mean bulk flow velocity of 5 m/s, those related to 25 m/s show that the non-swirling nozzle (which generates mixtures that feature stronger stratification, see the last column of Table 3), leads to PDF of $OH_{PLIF} \times CH_2O_{PLIF}$ integral with most probable value that is about 23% larger than that of the swirling nozzle. The reason for this is speculated to be linked to the number of pixels that feature significant $OH_{PLIF} \times CH_2O_{PLIF}$ for the non-swirling nozzle compared to the swirling nozzle at $U_0 = 25$ m/s. In order to investigate this, all $OH_{PLIF} \times CH_2O_{PLIF}$ results where binarized. Specifically, pixels featuring non-zero value of $OH_{PLIF} \times CH_2O_{PLIF}$ were assigned a unity value and the rest were set to zero. These binarized images related to the results presented in Fig. 10c, f, i, and l are shown in Fig. 21a–d, respectively. For each frame, the total number of pixels associated with the reaction layer were calculated and is referred to as n. The PDFs of n, for all tested conditions, are presented in Fig. 21e. The integral of $OH_{PLIF} \times CH_2O_{PLIF}$ divided by n was estimated. This ratio, which represents the intensity of the PLIF signals multiplication integral is shown in Fig. 21f. The results presented in Fig. 21e, f can be generally influenced by lack of accuracy in registration of the PLIF signals, the threshold value used for reduction of $OH_{PLIF} \times CH_2O_{PLIF}$, as well as the size of the median-based filters. The effects of these parameters on n as well as the intensity of

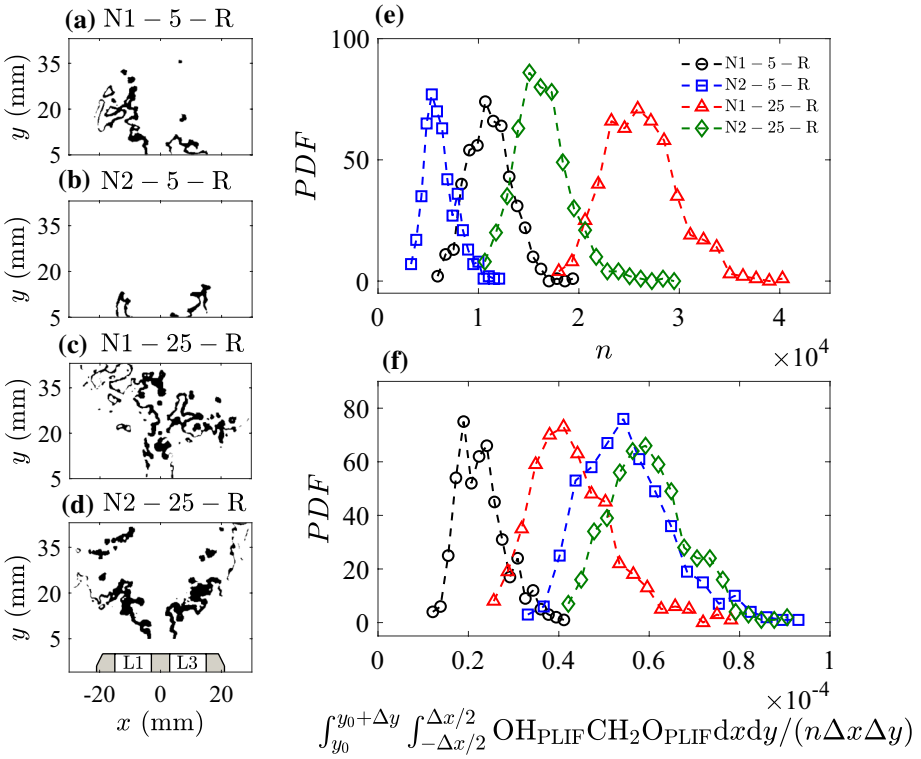

Fig. 21 **a–d** are the binarized $OH_{PLIF} \times CH_2O_{PLIF}$ frames shown in Fig. 10c, f, i, and l, respectively. **e** is the probability density function of the number of pixels with non-zero $OH_{PLIF} \times CH_2O_{PLIF}$, and **f** is the probability density function of the intensity of PLIF signals multiplication

$OH_{PLIF} \times CH_2O_{PLIF}$ are discussed in Appendix B. The results in Fig. 21e, f suggest that flames generated by the swirling nozzle and at 5 m/s feature the smallest most probable value of n and relatively large most probable value of $OH_{PLIF} \times CH_2O_{PLIF}$ intensity. This is linked to the large fuel–air equivalence ratio of lobe 1 for this condition compared to the rest of the tested conditions. It is important to note, despite featuring the fuel escape and later burning downstream for N1–5–R condition (as presented by the dashed boxes in Fig. 11a), this condition features the second smallest number of pixels with non-zero $OH_{PLIF} \times CH_2O_{PLIF}$ signal. This suggests the fuel escape and burning downstream does not contribute significantly to the intensity and integral of the PLIF signals multiplication. This observation is in agreement with the DNS results presented in Haworth et al. (2000) for stratified propane air flames.

The results in Fig. 21e suggest that the non-swirling nozzle features the largest most probable value of n at $U_0 = 25$ m/s. This is speculated to be linked to the frequent spatial occurrence of fragmented and pocket-like reaction zones, see Fig. 10i. In order to investigate this, the area of the reaction zones pertaining to each pixel shown in Fig. 21a–d were obtained and is referred to as A. Then, the probability density function of A was estimated for all frames, and the results are shown in Fig. 22. The inset of the figure shows an exemplary area A. As can be seen, the frequency of occurrence of a fragmented area is the largest for condition N1–25–R followed by N2–25–R, N1–5–R, and N2–5–R. This suggests, not only the non-swirling nozzle at $U_0 = 25$ m/s features the largest number of pixels with significant $OH_{PLIF} \times CH_2O_{PLIF}$, this nozzle features the largest occurrence of fragmented reaction zones compared to the rest of the tested conditions.

The results presented in the last column of Table 3 show that the non-swirling nozzle features stratification that is about 33% larger than the swirling nozzle at $U_0 = 25$ m/s. Also, the results presented in Table 3 show that moving from lobe 1 to 3, $\bar{\bar{r}}$ increases from about 0.7 to 1.3 for N1–25–NR, but it decreases from about 1.1 to 0.9 for N2–25–NR. The strong amount of stratification that exists for the non-swirling nozzle and at the mean bulk the flow velocity of 25 m/s may lead to the transport of fuel from the right-hand-side (lobe 3) to the left-hand-side (lobe 1). Since the combustion products are available at $x = 0$, this excess fuel is reignited leading to enhanced values of $OH_{PLIF} \times CH_2O_{PLIF}$ near $x = 0$ in Figs. 10 and 11i.

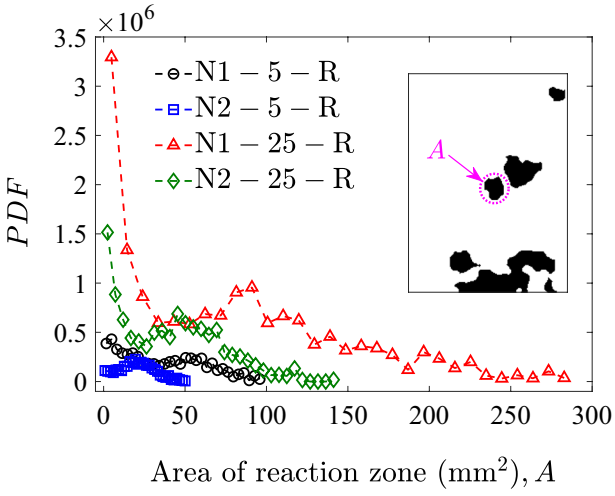

Fig. 22 The probability density function of the fragmented reaction zone area

Both stratification and turbulence are present for all tested conditions. These parameters are related, and it is not possible to isolate their respective effects on $OH_{PLIF} \times CH_2O_{PLIF}$ signals in the present study. However, comparisons can be made and conclusions can be drawn using the most probable values of the PDFs presented in Figs. 20 and 21. Aiming to address this, first, variation of $|\sigma_{13}| + |\sigma_{24}|$ (related to the strength of stratification) versus turbulence intensity is presented in Fig. 23a. As can be seen, increasing the mean bulk flow velocity and/or using the swirling nozzle decreases the amount of stratification. Specifically, at the largest tested mean bulk flow velocity (25 m/s), the non-swirling nozzle features larger amount of stratification compared to the swirling nozzle. Variations of the most probable values of the $OH_{PLIF} \times CH_2O_{PLIF}$ integral, the number of pixels with significant amount of the PLIF signals multiplication, and $OH_{PLIF} \times CH_2O_{PLIF}$ integral intensity are extracted from Figs. 20 and 21 and are shown in Fig. 23b–d, respectively. The error bars in Fig. 23 are the full-width at half maximum (FWHM) of the PDFs shown in Fig. 23. As can be seen, for both tested nozzles, increasing the mean bulk flow velocity increases the most probable values of the $OH_{PLIF} \times CH_2O_{PLIF}$ integral and intensity as well as n. The results show that, for both tested mean bulk flow velocities, the most probable value of number of pixels with significant $OH_{PLIF} \times CH_2O_{PLIF}$ is larger for the non-swirling nozzle compared to the swirling nozzle (see Fig. 23c). At the largest tested mean bulk flow velocity, the most probable value of the $OH_{PLIF} \times CH_2O_{PLIF}$ integral is also larger for the non-swirling nozzle compared to swirling nozzle (see Fig. 23b). Figure 23d also suggests that, at a given mean bulk flow velocity, the swirling nozzle (N2) features a larger $OH_{PLIF} \times CH_2O_{PLIF}$ intensity compared to the non-swirling nozzle (N1). This is linked to the larger eddy kinetic energy of N2 compared to N1 (see Figs. 16–19). In essence, the results presented in Fig. 23 for the largest tested mean bulk flow velocity suggest, despite using a non-swirling nozzle induces

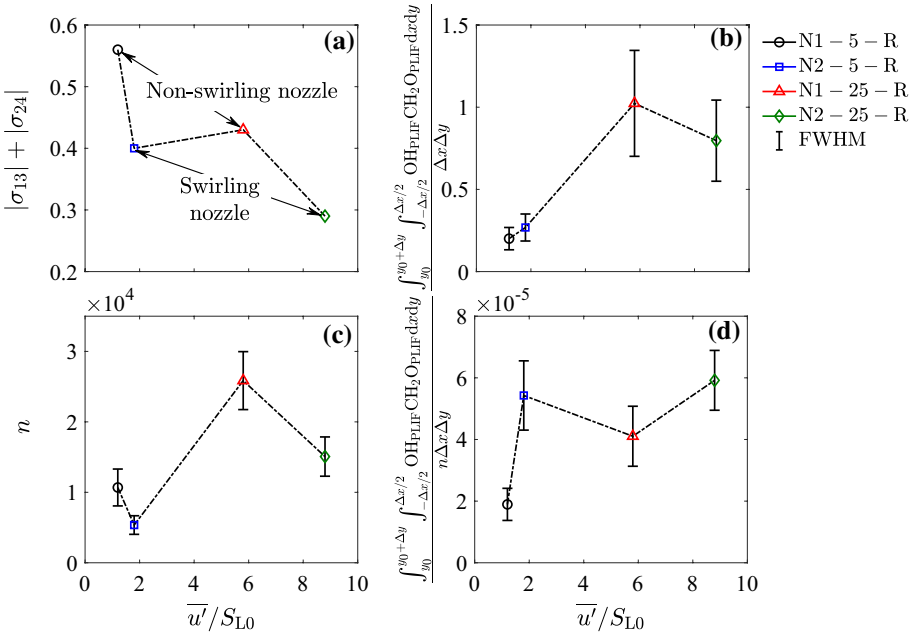

Fig. 23 **a** The strength of stratification versus the turbulence intensity. **b–d** are the most probable values of $OH_{PLIF} \times CH_2O_{PLIF}$ integral, n, and intensity of $OH_{PLIF} \times CH_2O_{PLIF}$, respectively

a relatively smaller turbulence intensity (compared to the swirling nozzle), the stratification is enhanced, the number of pixels with significant $OH_{PLIF} \times CH_2O_{PLIF}$ is increased, and as a result, $OH_{PLIF} \times CH_2O_{PLIF}$ integral features relatively large values.

5 Summary and Conclusions

The OH and formaldehyde PLIF signals multiplication of turbulent premixed flames with compositionally inhomogeneous mixtures was investigated experimentally. Two nozzles were utilized in the experiments. Each nozzle was composed of 4 injection lobes. The lobes of the first nozzle are straight; however, those of the second nozzle are not straight, allowing for generation of a swirling flow at the nozzle exit. Hydrogen-enriched methane (60% enrichment by volume) was used as the fuel. The fuel–air equivalence ratio was set to 0.8. Methane and hydrogen are perfectly mixed and then injected through small holes and into the lobes. The fuel and air are mixed locally, but the fuel–air equivalence ratio varies spatially. Two mean bulk flow velocities of 5 and 25 m/s were tested for each nozzle, leading to four reacting test conditions. For all reacting conditions, simultaneous Planar Laser-Induced Fluorescence (PLIF) of OH and CH_2O measurements as well as separate Stereoscopic Particle Image Velocimetry (SPIV) were performed. SPIV experiments were conducted separately for non-reacting conditions and for mean bulk flow velocities associated with each nozzle matching those of the reacting conditions. Separate acetone-PLIF experiments of the non-reacting conditions were also performed to investigate the amount of stratification for each test condition.

Using the acetone-PLIF of the non-reacting flow, the spatial distribution of the fuel–air equivalence ratio generated by each lobe was estimated. It was shown that for both tested mean bulk flow velocities, lobe 3 of of the non-swirling nozzle ejects richer mixture compared to lobe 1. For the swirling nozzle and at mean bulk flow velocity of 5 m/s, the opposite observation is made. At 25 m/s, the swirling nozzle generates a mixture that is nearly homogeneous.

The results show that, depending on the tested condition, the flames may be fully or partially anchored. A detailed characterization of the turbulent flow was performed. The specific kinetic energy of the eddies due to swirling motion was estimated. It was shown that the time-averaged value of this parameter is relatively large near the recirculation zones as well as those downstream of the averaged flame contour. While the former regions can potentially contribute to enhanced multiplication of OH and formaldehyde PLIF signals, the latter are due to the flame generated turbulence. Variation of the specific eddy kinetic energy due to swirling motion suggest the swirling nozzle generates larger number of energetic eddies. This was shown to be consistent with the RMS velocity calculations.

For the smaller tested mean bulk flow velocity, the swirling nozzle features an enhanced multiplication of OH and formaldehyde PLIF signals compared to the non-swirling nozzle. It is shown this is related to the enhanced laminar flame speed, which is a result of stratification. However, an opposite behavior is observed for the larger mean bulk flow velocity. Specifically, the non-swirling nozzle, despite ejecting a relatively leaner mixture and smaller turbulence intensity compared to the swirling nozzle, features a larger integral of the PLIF signals multiplication. This was argued to be linked to the flame structure. Specifically, at 25 m/s and for the non-swirling nozzle, the reaction layers are fragmented and occupy a relatively large area in the domain of investigation. This characteristic is not reported for stratified flames before to our best of

knowledge, and it is shown to lead to the reported larger integral of $OH_{PLIF} \times CH_2O_{PLIF}$. In essence, it is concluded that, although homogeneous premixing of fuel and air can potentially address several issues related to gaseous fuel combustion, stratification can generate flame structures that enhance the multiplication of OH and formaldehyde PLIF signals compared to that of the homogeneous premixed flame counterpart. The relation between this multiplication and the true heat release rate/burning rate is a matter of future investigations.

Appendix A: Assessing Accuracy of PLIF Images Registration

In addition to the method related to the three-dimensional target plate discussed in Sect. 2, an alternative method was also used to assess the utilized registration technique. Specifically, a perforated and back-illuminated plate was used for the alternative registration technique, similar to Mohammadnejad et al. (2019). This plate is composed of 225 small diameter (less than 0.5 mm) through holes. The perforated plate was positioned at the burner exit plane ($x-y$ plane) and equidistant from both OH and formaldehyde cameras. The plate was back illuminated for both of the cameras, and an image was acquired by each camera. The small diameter holes serve as local light sources, whose positions are captured by both cameras. The images of these small light sources were collected by both the CH_2O and OH cameras and are shown by the cyan and green data points in Fig. 24a. In the figure, the overlap between the collected light (which is obtained by multiplying the OH and CH_2O camera images) is shown by the red colored pixels. An inset, highlighting the overlap in Fig. 24a, is enlarged and shown in Fig. 24c. Lack of overlap between the images prior to registration can be seen. The images from both cameras were anlalyzed using the "imwrap" function in MATLAB, and the CH_2O images were mapped onto the OH images. The results after registration are shown in Fig. 24b, with an inset shown in Fig. 24d. As can be seen, proper registration was achieved. Identical results were obtained using this alternative registration method and the three-dimensional target plate.

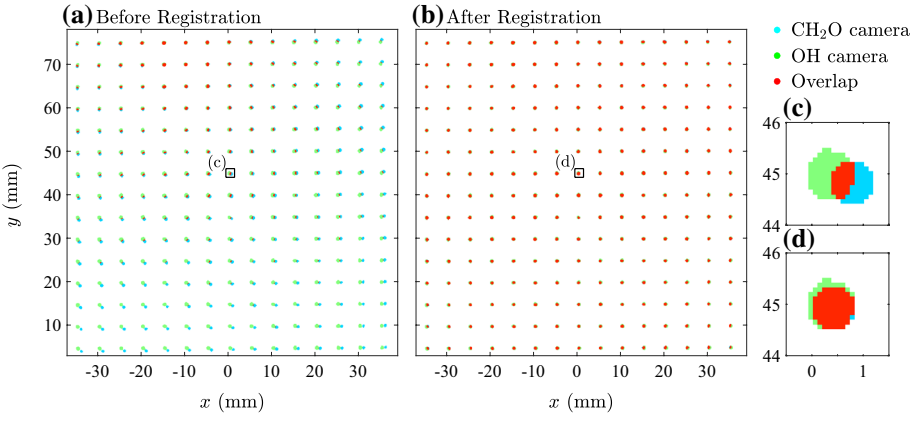

Fig. 24 **a** and **b** are images of a perforated and back-illuminated plate before and after registration, respectively. **c** and **d** are insets of (**a**) and (**b**), respectively

Appendix B: Sensitivity of $OH_{PLIF} \times CH_2O_{PLIF}$ to Registration, Global Thresholding, and Median-Based Filters

Effects of lack of accuracy in registration of the PLIF signals, varying the global threshold used in reduction of $OH_{PLIF} \times CH_2O_{PLIF}$ images, as well as the size of the median-based filters used for removing "salt-and-pepper" noise from the PLIF images on the results presented in Figs. 20 and 21 are discussed here.

The registered CH_2O PLIF images were displaced by one pixel towards left and right, the integral of $OH_{PLIF} \times CH_2O_{PLIF}$, n, and $OH_{PLIF} \times CH_2O_{PLIF}$ intensity were obtained, and the results were presented in Fig. 25a–c, respectively. For clarity purposes, only results pertaining to the smallest and largest Karlovitz numbers are presented in the figures. As can be seen, moving the registered CH_2O PLIF images towards left and right by one pixel does not significantly influence the PDFs of $OH_{PLIF} \times CH_2O_{PLIF}$ integral and intensity. The results show displacing the CH_2O_{PLIF} PLIF images towards right moves the PDF of n towards left (smaller values of n). However, analyses of all test conditions show that the changes in the PDFs of n are significantly small, which do not influence the conclusions of the study.

Changing the global threshold used for reducing the $OH_{PLIF} \times CH_2O_{PLIF}$ images can influence the results presented Figs. 20 and 21e, f. However, our analyses show that the reported trends and conclusions do not change by changing the value of the utilized threshold. In order to investigate this, compared to the 30% threshold value used for generating results in Figs. 20 and 21e, f, 20% and 40% threshold values were also used and the results in Figs. 20 and 21e, f were reproduced. The results associated with the integral of $OH_{PLIF} \times CH_2O_{PLIF}$, the number of pixels with significant $OH_{PLIF} \times CH_2O_{PLIF}$, and the intensity of $OH_{PLIF} \times CH_2O_{PLIF}$ are generated for all test conditions and are presented in Fig. 26a–c, respectively. The results related to 20% and 40% threshold values are shown by the dashed and solid curves, respectively. As can be seen, increasing the threshold value decreases the most probable value of $OH_{PLIF} \times CH_2O_{PLIF}$ integral and n, which is due to removing data when the large threshold value is applied. However, increasing the threshold value increases the most probable $OH_{PLIF} \times CH_2O_{PLIF}$ intensity. Nevertheless, the results presented in Fig. 26 show that changing the threshold value from 20% to 40% does not influence the relative relations between the most probable values of $OH_{PLIF} \times CH_2O_{PLIF}$ integral and intensity as well as n. For example, the

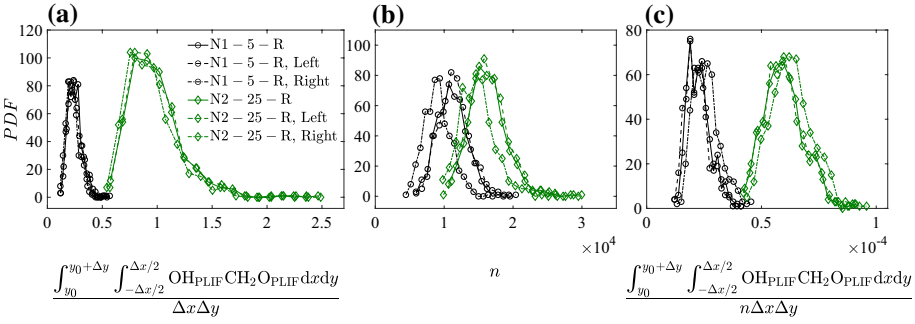

Fig. 25 PDFs of **a** $OH_{PLIF} \times CH_2O_{PLIF}$ integral, **b** n, and **c** $OH_{PLIF} \times CH_2O_{PLIF}$ intensity. In the figure legend, left and right pertain to the registered formaldehyde images displaced by one pixel to left and right

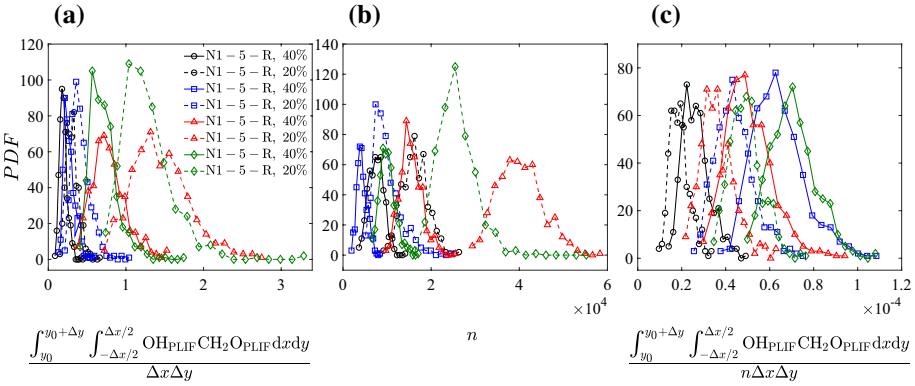

Fig. 26 Effects of threshold on **a** $OH_{PLIF} \times CH_2O_{PLIF}$ integral, **b** n, and **c** $OH_{PLIF} \times CH_2O_{PLIF}$ intensity

non-swirling nozzle at the mean bulk flow velocity of 25 m/s always features the largest most probable value of $OH_{PLIF} \times CH_2O_{PLIF}$ integral.

Median-based filters with 7×7 and 9×9 pixels^2 windows for filtering the OH and CH_2O PLIF images were used in the present study, respectively. Our analyses suggest changing the filter size does not influence the results presented in Figs. 20 and 21e, f. Figures 27a–c, present variations of the integral of $OH_{PLIF} \times CH_2O_{PLIF}$, n, and the $OH_{PLIF} \times CH_2O_{PLIF}$ intensity, respectively. The results highlighted by the solid curves pertain to the OH and CH_2O PLIF images filtered by 7×7 and 9×9 median-based filters, respectively. The results shown by the dashed curves pertain to OH and CH_2O PLIF images filtered by smaller windows of 5×5 and 7×7 median-based filters, respectively. As can be seen, reducing the filter size does not significantly influence the PDFs presented in Fig. 27.

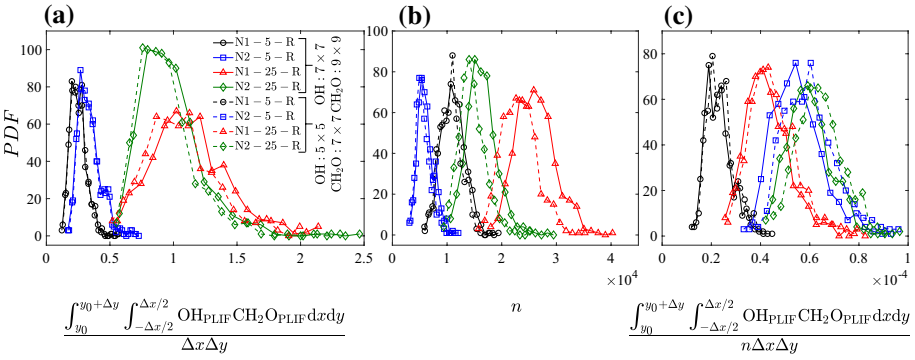

Fig. 27 **a–c** are variations of $OH_{PLIF} \times CH_2O_{PLIF}$ integral, n, and $OH_{PLIF} \times CH_2O_{PLIF}$ intensity, respectively. The solid curves pertain to OH and CH_2O filtered by 7×7 and 9×9 median-based filters; and, the dashed curves pertain to OH and CH_2O filtered by 5×5 and 7×7 median-based filters

Table 4 Uncertainties of the velocity data statistics along with the swirling strength and the eddy turbulent kinetic energy

Condition	U	V	W	u'	v'	w'	Q	T_Q
N1–5–NR	0.02	0.01	0.03	0.02	0.01	0.02	10^4	1.3
N2–5–NR	0.01	0.02	0.03	0.05	0.11	0.05	13×10^4	0.4
N1–25–NR	0.06	0.19	0.17	0.14	0.09	0.12	45×10^4	4.5
N2-25-NR	0.11	0.18	0.27	0.44	0.35	0.24	110×10^4	2.7
Max percentile	1%	1%	1%	10%	13%	6%	11%	7%

The unit of U, V, W, u', v', and w' is m/s. The units of Q and T_Q are s^{-2} and J/kg, respectively

Appendix C: Uncertainty of the Velocity Data and the Related Statistics

The uncertainties related to estimation of the velocity data, the swirling strength, and the eddy turbulent kinetic energy are provided in Table 4. For all parameters listed below, the statistical uncertainty is negligible. The uncertainties listed in Table 4 were obtained considering the repeatability of the experiments. In order to estimate the velocity data and the related parameters uncertainties, the repeatability of each parameter provided below was calculated by dividing the velocity data into three sets and calculating the maximum deviation of the mean. The results provided in the table are listed based on the tested condition. The last row of the table presents the maximum percentile of the uncertainty by finding the maximum (among all tested conditions) of the uncertainty divided by the mean value of the parameter of interest. For V and W, since the mean value can be close to zero, the uncertainty is divided by the corresponding U value.

Acknowledgements The authors are grateful for financial support from Siemens Energy Canada Ltd, the Mitacs Accelerate program (Funding Ref. #FR42789 awarded to the corresponding author), and the Gas Turbine Laboratory of the National Research Council Canada. Also, the authors would like to thank Professor Matthew Johnson (from the Carleton University) and Dr. Greg Smallwood (from NRC) for generously lending the optical equipment.

Declarations

Conflict of interest None.

References

Ahmed, S.F., Balachandran, R., Mastorakos, E.: Measurements of ignition probability in turbulent non-premixed counterflow flames. Proc. Combust. Inst. **31**(1), 1507–1513 (2007)

Anselmo-Filho, P., Hochgreb, S., Barlow, R., Cant, R.: Experimental measurements of geometric properties of turbulent stratified flames. Proc. Combust. Inst. **32**(2), 1763–1770 (2009)

Aspden, A., Day, M., Bell, J.: Lewis number effects in distributed flames. Proc. Combust. Inst. **33**(1), 1473–1480 (2011a)

Aspden, A., Day, M., Bell, J.: Turbulence-flame interactions in lean premixed hydrogen: transition to the distributed burning regime. J. Fluid Mech. **680**, 287–320 (2011b)

Aspden, A., Day, M., Bell, J.: Towards the distributed burning regime in turbulent premixed flames. J. Fluid Mech. **871**, 1–21 (2019)

Ayoola, B., Balachandran, R., Frank, J., Mastorakos, E., Kaminski, C.: Spatially resolved heat release rate measurements in turbulent premixed flames. Combust. Flame **144**(1–2), 1–16 (2006)

Ayoola, B., Hartung, G., Armitage, C.A., Hult, J., Cant, R.S., Kaminski, C.F.: Temperature response of turbulent premixed flames to inlet velocity oscillations. Exp. Fluids **46**(1), 27 (2009)
Böhm, B., Geyer, D., Dreizler, A., Venkatesan, K.K., Laurendeau, N.M., Renfro, M.W.: Simultaneous PIV/PTV/OH PLIF imaging: conditional flow field statistics in partially premixed turbulent opposed jet flames. Proc. Combust. Inst. **31**(1), 709–717 (2007)
Böhm, B., Frank, J., Dreizler, A.: Temperature and mixing field measurements in stratified lean premixed turbulent flames. Proc. Combust. Inst. **33**(1), 1583–1590 (2011)
Bonaldo, A., Kelman, J.: Experimental annular stratified flames characterisation stabilised by weak swirl. Combust. Flame **156**(4), 750–762 (2009)
Borghi, R.: Turbulent combustion modelling. Prog. Energy Combust. Sci. **14**(4), 245–292 (1988)
Bourguignon, E., Kostiuk, L., Michou, Y., Gökalp, I.: Experimentally measured burning rates of premixed turbulent flames. Proc. Combust. Inst. **26**(1), 447–453 (1996)
Brackmann, C., Nygren, J., Bai, X., Li, Z., Bladh, H., Axelsson, B., Denbratt, I., Koopmans, L., Bengtsson, P.E., Aldén, M.: Laser-induced fluorescence of formaldehyde in combustion using third harmonic Nd:YAG laser excitation. Spectrochim. Acta Part A Mol. Biomol. Spectrosc. **59**(14), 3347–3356 (2003)
Candel, S.: Combustion instabilities coupled by pressure waves and their active control. Proc. Combust. Inst. **24**(1), 1277–1296 (1992)
Carter, C.D., Hammack, S., Lee, T.: High-speed flamefront imaging in premixed turbulent flames using planar laser-induced fluorescence of the CH C-X band. Combust. Flame **168**, 66–74 (2016)
Cho, Y.S., Santavicca, D.A.: The effect of incomplete fuel-air mixing on spark-ignited flame kernel growth, SAE Technical Paper 932715 (1993)
Clemens, N.: Flow imaging, encyclopedia of imaging science and technology. Wiley, London (2002)
Cucitore, R., Quadrio, M., Baron, A.: On the effectiveness and limitations of local criteria for the identification of a vortex. Eur. J. Mech. B Fluids **18**(2), 261–282 (1999)
Degardin, O., Renou, B., Boukhalfa, A.: Simultaneous measurement of temperature and fuel mole fraction using acetone planar induced fluorescence and Rayleigh scattering in stratified flames. Exp. Fluids **40**(3), 452–463 (2006)
Driscoll, J.: Turbulent premixed combustion: flamelet structure and its effect on turbulent burning velocities. Prog. Energy Combust. Sci. **34**(1), 91–134 (2008)
Driscoll, J., Chen, J., Skiba, A., Carter, C., Hawkes, E., Wang, H.: Premixed flames subjected to extreme turbulence: some questions and recent answers. Prog. Energy Combust. Sci. **76**, 100802 (2020)
Dunn, M., Masri, A., Bilger, R.: A new piloted premixed jet burner to study strong finite-rate chemistry effects. Combust. Flame **151**(1–2), 46–60 (2007)
Dunn, M., Masri, A., Bilger, R., Barlow, R., Wang, G.: The compositional structure of highly turbulent piloted premixed flames issuing into a hot coflow. Proc. Combust. Inst. **32**(2), 1779–1786 (2009)
Dunn, M., Masri, A., Bilger, R., Barlow, R.: Finite rate chemistry effects in highly sheared turbulent premixed flames. Flow Turbul. Combust. **85**(3–4), 621–648 (2010)
Eckbreth, A.: Laser Diagnostics for Combustion Temperature and Species, vol. 3. CRC Press, London (1996)
Elbaz, A.M., Roberts, W.L.: Experimental study of the inverse diffusion flame using high repetition rate OH/acetone PLIF and PIV. Fuel **165**, 447–461 (2016)
Fayoux, A., Zähringer, K., Gicquel, O., Rolon, J.: Experimental and numerical determination of heat release in counterflow premixed laminar flames. Proc. Combust. Inst. **30**(1), 251–257 (2005)
Filatyev, S.A., Driscoll, J.F., Carter, C.D., Donbar, J.M.: Measured properties of turbulent premixed flames for model assessment, including burning velocities, stretch rates, and surface densities. Combust. Flame **141**(1–2), 1–21 (2005)
Galizzi, C., Escudié, D.: Experimental analysis of an oblique turbulent flame front propagating in a stratified flow. Combust. Flame **157**(12), 2277–2285 (2010)
Goodwin, D.G., Speth, R.L., Moffat, H.K., Weber, B.W.: Cantera: An Object-Oriented Software Toolkit for Chemical Kinetics, Thermodynamics, and Transport Processes. https://www.cantera.org, version 2.4.0 (2018)
Gouldin, F., Miles, P.: Chemical closure and burning rates in premixed turbulent flames. Combust. Flame **100**(1–2), 202–210 (1995)
Gülder, Ö.: Contribution of small scale turbulence to burning velocity of flamelets in the thin reaction zone regime. Proc. Combust. Inst. **31**(1), 1369–1375 (2007)
Guo, H., Tayebi, B., Galizzi, C., Escudié, D.: Burning rates and surface characteristics of hydrogen-enriched turbulent lean premixed methane-air flames. Int. J. Hydrog. Energy **35**(20), 11342–11348 (2010)
Hardalupas, Y., Panoutsos, C.S., Taylor, A.: Spatial resolution of a chemiluminescence sensor for local heat-release rate and equivalence ratio measurements in a model gas turbine combustor. Exp. Fluids **49**(4), 883–909 (2010)

Harrington, J., Smyth, K.: Laser-induced fluorescence measurements of formaldehyde in a methane/air diffusion flame. Chem. Phys. Lett. **202**(3–4), 196–202 (1993)
Haworth, D., Blint, R., Cuenot, B., Poinsot, T.: Numerical simulation of turbulent propane-air combustion with nonhomogeneous reactants. Combust. Flame **121**(3), 395–417 (2000)
Hewson, J., Bollig, M.: Reduced mechanisms for NOx emissions from hydrocarbon diffusion flames. Proc. Combust. Inst. **26**(2), 2171–2179 (1996)
Huang, Y., Yang, V.: Effect of swirl on combustion dynamics in a lean-premixed swirl-stabilized combustor. Proc. Combust. Inst. **30**(2), 1775–1782 (2005)
Jeong, J., Hussain, F.: On the identification of a vortex. J. Fluid Mech. **285**, 69–94 (1995)
Kheirkhah, S.: Experimental study of turbulent premixed combustion in V-shaped flames. Ph.D. thesis, The University of Toronto (2016)
Kheirkhah, S., Gülder, Ö.: Turbulent premixed combustion in V-shaped flames: characteristics of flame front. Phys. Fluids **25**(5), 055107 (2013)
Kheirkhah, S., Gülder, Ö.: Consumption speed and burning velocity in counter-gradient and gradient diffusion regimes of turbulent premixed combustion. Combust. Flame **162**(4), 1422–1439 (2015)
Kohse-Höinghaus, K., Jeffries, J.B.: Applied combustion diagnostics (2002)
Lapointe, S., Savard, B., Blanquart, G.: Differential diffusion effects, distributed burning, and local extinctions in high Karlovitz premixed flames. Combust. Flame **162**(9), 3341–3355 (2015)
Lieuwen, T.: Modeling premixed combustion-acoustic wave interactions: a review. J. Propul. Power **19**(5), 765–781 (2003)
Masri, A.: Partial premixing and stratification in turbulent flames. Proc. Combust. Inst. **35**(2), 1115–1136 (2015)
McManus, K., Poinsot, T., Candel, S.M.: A review of active control of combustion instabilities. Prog. Energy Combust. Sci. **19**(1), 1–29 (1993)
Mohammadnejad, S., Vena, P., Yun, S., Kheirkhah, S.: Internal structure of hydrogen-enriched methane-air turbulent premixed flames: flamelet and non-flamelet behavior. Combust. Flame **208**, 139–157 (2019)
Mohammadnejad, S., An, Q., Vena, P., Yun, S., Kheirkhah, S.: Thick reaction zones in non-flamelet turbulent premixed combustion. Combust. Flame **222**, 285–304 (2020)
Moore, M.: NOx emission control in gas turbines for combined cycle gas turbine plant. Proc. Inst. Mech. Eng. Part A J. Power Energy **211**(1), 43–52 (1997)
Najm, H., Knio, O., Paul, P., Wyckoff, P.: A study of flame observables in premixed methane-air flames. Combust. Sci. Technol. **140**(1–6), 369–403 (1998)
Najm, H., Paul, P., Mueller, C., Wyckoff, P.: On the adequacy of certain experimental observables as measurements of flame burning rate. Combust. Flame **113**(3), 312–332 (1998)
O'Connor, J., Lieuwen, T.: Recirculation zone dynamics of a transversely excited swirl flow and flame. Phys. Fluids **24**(7), 2893–2900 (2012)
Osborne, J.R., Ramji, S.A., Carter, C.D., Peltier, S., Hammack, S., Lee, T., Steinberg, A.M.: Simultaneous 10 kHz TPIV, OH PLIF, and CH2O PLIF measurements of turbulent flame structure and dynamics. Exp. Fluids **57**(5), 65 (2016)
Pasquier, N., Lecordier, B., Trinite, M., Cessou, A.: An experimental investigation of flame propagation through a turbulent stratified mixture. Proc. Combust. Inst. **31**(1), 1567–1574 (2007)
Paul, P., Najm, H.: Planar laser-induced fluorescence imaging of flame heat release rate. Proc. Combust. Inst. **27**(1), 43–50 (1998)
Peters, N.: Turbulent Combustion. Cambridge University Press, Cambridge (2000)
Plessing, T., Kortschik, C., Peters, N., Mansour, M., Cheng, R.: Measurements of the turbulent burning velocity and the structure of premixed flames on a low-swirl burner. Proc. Combust. Inst. **28**(1), 359–366 (2000)
Pope, S.: Turbulent flows. IOP Publishing, New York (2001)
Robin, V., Mura, A., Champion, M., Degardin, O., Renou, B., Boukhalfa, M.: Experimental and numerical analysis of stratified turbulent V-shaped flames. Combust. Flame **153**(1–2), 288–315 (2008)
Seffrin, F., Fuest, F., Geyer, D., Dreizler, A.: Flow field studies of a new series of turbulent premixed stratified flames. Combust. Flame **157**(2), 384–396 (2010)
Sheen, H., Chen, W., Jeng, S.: Recirculation zones of unconfined and confined annular swirling jets. AIAA J. **34**(3), 572–579 (1996)
Sjöholm, J., Rosell, J., Li, B., Richter, M., Li, Z., Bai, X.-S., Aldén, M.: Simultaneous visualization of OH, CH, CH2O and toluene PLIF in a methane jet flame with varying degrees of turbulence. Proc. Combust. Inst. **34**(1), 1475–1482 (2013)
Skiba, A., Wabel, T., Temme, J., Driscoll, J.: Experimental assessment of premixed flames subjected to extreme turbulence. In: 54th AIAA Aerospace Sciences Meeting 1454 (2016)

Skiba, A.: On the structure of premixed flames subjected to extreme levels of turbulence. Ph.D. thesis, The University of Michigan (2017)
Skiba, A.W., Wabel, T.M., Carter, C.D., Hammack, S.D., Temme, J.E., Lee, T., Driscoll, J.F.: Reaction layer visualization: a comparison of two PLIF techniques and advantages of kHz-imaging. Proc. Combust. Inst. **36**(3), 4593–4601 (2017)
Skiba, A., Wabel, T., Carter, C., Hammack, S., Temme, J., Driscoll, J.: Premixed flames subjected to extreme levels of turbulence part I: flame structure and a new measured regime diagram. Combust. Flame **189**, 407–432 (2018)
Skiba, A.W., Carter, C.D., Hammack, S.D., Miller, J.D., Gord, J., Driscoll, J.: The influence of large eddies on the structure of turbulent premixed flames characterized with stereo-PIV and multi-species PLIF at 20 kHz. Proc. Combust. Inst. **37**(2), 2477–2484 (2019)
Sweeney, M., Hochgreb, S., Barlow, R.: The structure of premixed and stratified low turbulence flames. Combust. Flame **158**(5), 935–948 (2011a)
Sweeney, M., Hochgreb, S., Dunn, M., Barlow, R.: A comparative analysis of flame surface density metrics inpremixed and stratified flames. Proc. Combust. Inst. **33**(1), 1419–1427 (2011b)
Sweeney, M., Hochgreb, S., Dunn, M., Barlow, R.: The structure of turbulent stratified and premixed methane/air flames II: swirling flows. Combust. Flame **159**(9), 2912–2929 (2012a)
Sweeney, M., Hochgreb, S., Dunn, M., Barlow, R.: The structure of turbulent stratified and premixed methane/air flames I: non-swirling flows. Combust. Flame **159**(9), 2896–2911 (2012b)
Tamadonfar, P., Gülder, Ö.: Effect of burner diameter on the burning velocity of premixed turbulent flames stabilized on Bunsen-type burners. Exp. Thermal Fluid Sci. **73**, 42–48 (2016)
Tamura, M., Berg, P.A., Harrington, J.E., Luque, J., Jeffries, J.B., Smith, G.P., Crosley, D.R.: Collisional quenching of CH(A), OH(A), and NO(A) in low pressure hydrocarbon flames. Combust. Flame **114**(3–4), 502–514 (1998)
Terasaki, T., Hayashi, S.: The effects of fuel-air mixing on NOx formation in non-premixed swirl burners. Proc. Combust. Inst. **26**(2), 2733–2739 (1996)
Turns, S.: An Introduction to Combustion. McGraw-Hill, New York (1996)
Vena, P., Deschamps, B., Guo, H., Smallwood, G., Johnson, M.: Heat release rate variations in a globally stoichiometric, stratified iso-octane/air turbulent V-flame. Combust. Flame **162**(4), 944–959 (2015a)
Vena, P., Deschamps, B., Guo, H., Johnson, M.: Effects of stratification on locally lean, near-stoichiometric, and rich iso-octane/air turbulent v-flames. Combust. Flame **162**(11), 4231–4240 (2015b)
Wabel, T., Zhang, P., Zhao, X., Wang, H., Hawkes, E., Steinberg, A.: Assessment of chemical scalars for heat release rate measurement in highly turbulent premixed combustion including experimental factors. Combust. Flame **194**, 485–506 (2018)
Wang, G., Clemens, N.: Effects of imaging system blur on measurements of flow scalars and scalar gradients. Exp. Fluids **37**(2), 194–205 (2004)
Wang, H., Hawkes, E., Chen, J., Zhou, B., Li, Z., Aldén, M.: Direct numerical simulations of a high Karlovitz number laboratory premixed jet flame-an analysis of flame stretch and flame thickening [direct numerical simulations of a high ka laboratory premixed jet flame-an analysis of flame stretch and flame thickening]. J. Fluid Mech. **815**, 511–536 (2017)
Wang, H., Hawkes, E., Savard, B., Chen, J.: Direct numerical simulation of a high Ka CH4/air stratified premixed jet flame. Combust. Flame **193**, 229–245 (2018)
Weinkauff, J., Trunk, P., Frank, J., Dunn, M., Dreizler, A., Böhm, B.: Investigation of flame propagation in a partially premixed jet by high-speed-Stereo-PIV and acetone-PLIF. Proc. Combust. Inst. **35**(3), 3773–3781 (2015)
Westerweel, J., Scarano, F.: Universal outlier detection for PIV data. Exp. Fluids **39**(6), 1096–1100 (2005)
Yamamoto, K., Isii, S., Ohnishi, M.: Local flame structure and turbulent burning velocity by joint PLIF imaging. Proc. Combust. Inst. **33**(1), 1285–1292 (2011)
Yan, B., Li, B., Baudoin, E., Liu, C., Sun, Z., Li, Z., Bai, X.-S., Aldén, M., Chen, G., Mansour, M.: Structures and stabilization of low calorific value gas turbulent partially premixed flames in a conical burner. Exp. Thermal Fluid Sci. **34**(3), 412–419 (2010)
Yuen, F., Gülder, Ö.: Premixed turbulent flame front structure investigation by Rayleigh scattering in the thin reaction zone regime. Proc. Combust. Inst. **32**(2), 1747–1754 (2009)
Zhou, J., Yoshizaki, T., Nishida, K., Hiroyasu, H.: Effects of mixture heterogeneity on flame propagation in a constant volume combustion chamber. SAE Trans. **106**, 1387–1402 (1997)
Zhou, B., Brackmann, C., Li, Q., Wang, Z., Petersson, P., Li, Z., Aldén, M., Bai, X.: Distributed reactions in highly turbulent premixed methane/air flames: part I. Flame structure characterization. Combust. Flame **162**(7), 2937–2953 (2015a)

Zhou, B., Brackmann, C., Li, Z., Aldén, M., Bai, X.: Simultaneous multi-species and temperature visualization of premixed flames in the distributed reaction zone regime. Proc. Combust. Inst. **35**(2), 1409–1416 (2015b)

Zhou, B., Brackmann, C., Wang, Z., Li, Z., Richter, M., Aldén, M., Bai, X.: Thin reaction zone and distributed reaction zone regimes in turbulent premixed methane/air flames: scalar distributions and correlations. Combust. Flame **175**, 220–236 (2017)

Zimont, V.: Theory of turbulent combustion of a homogeneous fuel mixture at high Reynolds numbers. Combust. Explos. Shock Waves **15**(3), 305–311 (1979)